Publications

6-25-2022

Modeling Studies of Gravity Wave Dynamics in Highly Structured Environments: Reflection, Trapping, Instability, Momentum Transport, Secondary Gravity Waves, and Induced Flow Responses

Wenjun Dong
Embry-Riddle Aeronautical University

David C. Fritts
Embry-Riddle Aeronautical University

Michael P. Hickey
Embry-Riddle Aeronautical University

Alan Z. Liu
Embry-Riddle Aeronautical University

Thomas S. Lund
University of Colorado, Boulder

Follow this and additional works at: https://commons.erau.edu/publication

See next page for additional authors

Part of the Atmospheric Sciences Commons

Scholarly Commons Citation

Dong, W., Fritts, D. C., Hickey, M. P., Liu, A. Z., Lund, T. S., Zhang, S., et al. (2022). Modeling studies of gravity wave dynamics in highly structured environments: Reflection, trapping, instability, momentum transport, secondary gravity waves, and induced flow responses. Journal of Geophysical Research: Atmospheres, 127, e2021JD035894. https://doi. org/10.1029/2021JD035894

Authors

Wenjun Dong, David C. Fritts, Michael P. Hickey, Alan Z. Liu, Thomas S. Lund, Shaodong Zhang, Yanying Yan, and Fan Yang

Correspondence to:
A. Z. Liu,
Liuz2@erau.edu

Modeling Studies of Gravity Wave Dynamics in Highly Structured Environments: Reflection, Trapping, Instability, Momentum Transport, Secondary Gravity Waves, and Induced Flow Responses

Wenjun Dong[1,2] , **David C. Fritts**[1,2] , **Michael P. Hickey**[2] , **Alan Z. Liu**[2] ,
Thomas S. Lund[1,3], **Shaodong Zhang**[4] , **Yanying Yan**[5] , and **Fan Yang**[2]

[1]Global Atmospheric Technologies and Sciences (GATS), Boulder, CO, USA, [2]Center for Space and Atmospheric Research (CSAR) and Department of Physical Sciences, Embry-Riddle Aeronautical University, Daytona Beach, FL, USA, [3]IRISS Grand Challenge, University of Colorado, Boulder, CO, USA, [4]School of Electronic Information, Wuhan University, Wuhan, China, [5]College of Data Science, Taiyuan University of Technology, Taiyuan, China

Abstract A compressible numerical model is applied for three-dimensional (3-D) gravity wave (GW) packets undergoing momentum deposition, self-acceleration (SA), breaking, and secondary GW (SGW) generation in the presence of highly-structured environments enabling thermal and/or Doppler ducts, such as a mesospheric inversion layer (MIL), tidal wind (TW), or combination of MIL and TW. Simulations reveal that ducts can strongly modulate GW dynamics. Responses modeled here include reflection, trapping, suppressed transmission, strong local instabilities, reduced SGW generations, higher altitude SGW responses, and induced large-scale flows. Instabilities that arise in ducts experience strong dissipation after they emerge, while trapped smaller-amplitude and smaller-scale GWs can survive in ducts to much later times. Additionally, GW breaking and its associated dynamics enhance the local wind along the GW propagation direction in the ducts, and yield layering in the wind field. However, these dynamics do not yield significant heat transport in the ducts. The failure of GW breaking to induce stratified layers in the temperature field suggests that such heat transport might not be as strong as previously assumed or inferred from observations and theoretical assessments. The present numerical simulations confirm previous finding that MIL generation may not be caused by the breaking of a transient high-frequency GW packet alone.

1. Introduction

Gravity waves (GWs) play a central role in the transfer of energy and momentum from the lower to the upper atmosphere (Fritts & Alexander, 2003). Their significance in forcing the mean state of the mesosphere and lower thermosphere (MLT) is acknowledged by inclusion of their influences via parameterization in all numerical weather prediction, climate, and general circulation models. Evidence of GW activity in the MLT exists in the wealth of airglow and polar mesospheric cloud (PMC) observations and simulations that detail horizontal scales and velocities of both vertically propagating and ducted GWs, and turbulence and instability events (e.g., Dong, Fritts, et al., 2021; Dong, Hickey, & Zhang, 2021; Fritts et al., 1993, 2019; Yue et al., 2009). GW signatures are also present in ground-based radar and lidar profiling (e.g., Baumgarten et al., 2017; Cao et al., 2016; Chen et al., 2016; Kaifler et al., 2017, 2020; Li et al., 2007), radiosondes (e.g., Murphy et al., 2014; Stephan et al., 2020; Tsuda et al., 2004; Zhang et al., 2013, 2014), MLT imaging (Baumgarten & Fritts, 2014; Fritts et al., 1993, 2019; Hecht et al., 2005, 2020; Pautet et al., 2014, 2021), and satellite-based imaging (e.g., Alexander & Barnet, 2007; Ern et al., 2011; Hindley et al., 2020; Liu et al., 2017) from which GW scales and approximate amplitudes can be deduced at various altitudes.

Because GW amplitudes grow approximately exponentially with altitude in the absence of dissipation to conserve wave action in an ambient medium with decreasing density, GWs can have important effects at higher altitudes even if initial amplitudes are small. GWs often achieve sufficiently large amplitudes that they become susceptible to a diversity of interactions and/or local instabilities. Idealized GW packets can exhibit parametric and modulational instabilities with sufficient time (Klostermeyer, 1991; Lombard & Riley, 1996; Sutherland, 2006). GW "self-acceleration" (hereafter SA, e.g., acceleration of the GW horizontal phase speed due to its residence in the region undergoing mean flow acceleration along its direction of propagation) arises because GW packets

Project Administration: David C. Fritts, Alan Z. Liu

Resources: David C. Fritts, Thomas S. Lund

Software: Wenjun Dong, Thomas S. Lund

Supervision: Wenjun Dong, David C. Fritts, Alan Z. Liu

Validation: Wenjun Dong, Michael P. Hickey, Alan Z. Liu, Yanying Yan, Fan Yang

Visualization: Wenjun Dong

Writing – original draft: Wenjun Dong

Writing – review & editing: David C. Fritts, Michael P. Hickey, Alan Z. Liu, Shaodong Zhang, Yanying Yan, Fan Yang

induce pseudo-momentum fluxes that distort the GW packets (Fritts & Dunkerton, 1984; Sutherland, 2001). SA dynamics appear to be the major GW "packet" instability at finite amplitudes (Sutherland, 2006), especially in the atmosphere in which GW amplitudes and induced GW SA dynamics increase exponentially with altitude (Dong et al., 2020; Fritts et al., 2015, 2020).

Transient GW pseudo-momentum flux convergence (divergence) accelerates (decelerates) the local mean flow along the GW propagation direction and distorts the GW phase. This causes the leading (trailing) GW phases to steepen (become shallower). Depending on the GW amplitude, its packet depth, its environment, and its induced accelerations, it can exhibit either (a) breaking approaching overturning amplitudes, (b) shear instabilities where these dynamics enhance local shears, (c) approach to a critical level that drives a decreasing vertical wavelength, λ_z, and small-scale shear instabilities or breaking, or (c) SA dynamics exhibiting different, larger-scale, and stronger instabilities and breaking. All of these dynamics can excite secondary GWs (SGWs), but the apparent strongest sources appear to be deep GW breaking (Lund et al., 2020) and SA dynamics of localized GW packets (Dong et al., 2020; Dong, Fritts, et al., 2021; Dong, Hickey, & Zhang, 2021; Fritts et al., 2020). In the case of SA dynamics, SGWs are excited in two ways. First, rapid pseudo-momentum flux convergence and divergence yield a rapidly increasing pseudo-momentum enhancement to the local mean flow, for example, a strong, transient, local ΔU in the direction of GW propagation that projects onto SGW scales dictated by the ΔU spatial scales, hence larger SGW scales. Importantly, this component of SGW generation occurs prior to primary GW SA instabilities and breaking. Second, as SA instabilities and breaking arise, these excite additional, smaller-scale SGWs and acoustic waves (AWs) that also radiate outward from the SA breaking event.

Our topics of interest here are the nonlinear responses to large-amplitude GWs encountering ducting environments. Highly structured wind fields enabling Doppler ducts, and highly-structured temperature fields enabling thermal ducts, or both, are suggested to serve as ducting environments for high-frequency GWs (e.g., Chimonas & Hines, 1986; Dong, Fritts, et al., 2021; Dong, Hickey, & Zhang, 2021; Dong et al., 2018; Fritts & Li, 1989; Heale et al., 2014; Snively & Pasko, 2004; Snively et al., 2007; Yu & Hickey, 2007a, 2007b). For a specified GW, ducts occur when two evanescence regions ($m^2 < 0$) sandwich a region of internal wave propagation ($m^2 > 0$). In general, Doppler ducts are controlled primarily by larger-scale dynamics, especially tidal and planetary wave winds, and are expected to be shorter lived due to the high variability of the winds over periods of a few hours (Larsen, 2002).

MILs often serve as thermal ducts for high-frequency GWs (e.g., Dewan & Picard, 1998; Dewan & Ricard, 2001; Walterscheid & Hickey, 2009). MILs are regions of enhanced static stability, N^2 (where N is the Brunt-Väisala frequency), resulting from local $T(z)$ maxima with amplitudes that can reach $20 \sim 30K$ or larger, relative to adjacent cooler regions. MILs are frequently observed in both single-site measurements (Hauchecorne et al., 1987) and satellite studies (Gan et al., 2012). The formation mechanisms of MILs are not fully understood and there have been multiple theories offered to date (Meriwether & Gardner, 2000), among them, GW breaking (Hauchecorne et al., 1987), nonlinear interactions between GWs and tides (Liu & Hagan, 1998; Liu et al., 2000), planetary waves (e.g., France et al., 2015), and chemical heating due to exothermic chemical reactions (Meriwether & Mlynczak, 1995).

In the middle atmosphere, the strongest GW activity usually occurs during high-latitude winter and low-latitude equinox (Meriwether & Gerrard, 2004). This coincides with where MILs are the strongest, suggesting a close linkage between GW breaking and the formation of MILs in some cases. Hauchecorne et al. (1987) proposed convective instability of GWs as the mechanism for generating MILs due to the heating of the turbulent layers generated by the continuous GW breaking. Huang et al. (1998) suggested that MILs are associated with energy deposition, direct and indirect, resulting from GW/critical layer interactions. A subsequent study by Huang et al. (2002) that included temperature gradients in the calculation of the Richardson number, $Ri = N^2/[(dU/dz)^2 + (dV/dz)^2]$, for local-mean zonal and meridional winds, U and V, showed that the atmosphere was more unstable than previously thought, providing support for their original hypothesis. Their calculations also showed that energy transported by the observed GW was sufficiently large to account for an increase of mean temperature. However, Duck et al. (2001) argued that GW breaking cannot provide sufficient heating rates to explain observed temperature enhancement causing MILs.

(Fritts, Laughman et al. (2018), Fritts, Wang ett al. (2018), hereafter F18) performed a series of MIL simulations for 1-D GW packets having ratios of vertical to horizontal wavelengths as large as 2 and associated intrinsic frequencies as high as 0.7 *N*. F18 results relevant to our current study include the following:

1. GW breaking and turbulence in the MIL occur below where they would otherwise arise, due to enhancements of GW amplitudes and shears in the MIL.
2. MILs intensify GW amplitudes and shears that can enable instabilities, turbulence, and GW dissipation at sufficient amplitudes. GW dissipation in a MIL yields energy and momentum deposition, jet formation, and reduced transmission and reflection.
3. 2-D and 3-D heat fluxes in regions of strong turbulence yield small departures from initial background temperature, and hence do not yield nearly adiabatic "mixed" layers.

In F18, the anelastic formulation prevented acoustic wave (AW) generation, and the assumption of horizontal periodicity in the horizontal direction, which limits GW packets to vary only in *z* direction, artificially constrained the spectrum of motions that can arise from nonlinear interactions and instability dynamics. In particular, spatial and temporal localization of GW packets plays key roles in the partitioning of body forces accompanying momentum transport among mean responses and SGW generation. These limitations were addressed by Fritts et al. (2020, hereafter F20), who examined a 3-D GW packet attaining amplitudes required by GW breaking in a representative 3-D tidal wind (TW) field. F20 results relevant to our current study include the following:

1. Localized 3-D GW packets exhibit strong SA dynamics, local 3-D instabilities and dissipation, and SGW and AW generation.
2. SGWs are modulated by TW and have large scales and large influences extending into the thermosphere. Responses include refraction by TW, and reduced SGW responses at higher altitudes relative to the case of no TW.
3. TW were found to constrain GW amplitudes, cause GW dissipation, momentum deposition, local body forces accompanying decreasing phase speeds, and to yield layering of induced mean responses.

The studies cited above have shown that nonlinear dynamics at small and large scales drive interactions, instabilities, and turbulent dissipation and hence play important roles in energy and momentum deposition, modulations of tides, and evolution of the GW spectrum throughout the atmosphere. They also reveal that a more quantitative understanding of GW dynamics and effects in highly structured atmospheres must address the related dynamics in 3-D. Motivated by these previous studies, we use a versatile compressible model to explore 3-D GWs undergoing strong SA and breaking dynamics in the presence of MIL, TW, or the combination of MIL and TW. This modeling study addresses three primary questions concerning multiscale GW environments:

1. What are the key dynamics in GW-MIL and GW-TW interactions for GW packets localized in 3-D?
2. How do MILs and TW affect the GW evolutions and the associated energy and momentum transports and energy exchanges among various GW components in the packet?
3. How do these dynamics affect the wind and thermal structure?

Our paper is organized as follows. Section 2 briefly describes the numerical model and simulation setup. The results and analyses are provided in Section 3. Section 4 discusses these results in relation to those of previous studies. A summary and our conclusions are provided in Section 5.

2. Numerical Model and Simulation Setup

2.1. Numerical Model

The numerical model used for our simulations is the Complex Geometry Compressible Atmosphere Model (CGCAM), which solves the 3-D fully nonlinear and compressible Navier-Stokes equations. These can be written in strong conservation law (flux) form as:

$$\frac{\partial \rho}{\partial t} + \frac{\partial (\rho u_j)}{\partial x_j} = 0 \tag{1}$$

$$\frac{\partial(\rho u_i)}{\partial t} + \frac{\partial(\rho u_i u_j)}{\partial x_j} = -\frac{\partial p}{\partial x_i} - \rho g \delta_{i3} + \frac{\partial \sigma_{ij}}{\partial x_j} \tag{2}$$

$$\frac{\partial(\rho E)}{\partial t} + \frac{\partial\left[(\rho E + p)u_j\right]}{\partial x_j} = -\rho g u_3 + \frac{\partial(u_i \sigma_{ij})}{\partial x_j} - \frac{\partial q_j}{\partial x_j} \tag{3}$$

where σ_{ij} and q_j are the viscous stress and thermal conduction, respectively, defined as

$$\sigma_{ij} = \mu\left[\left(\frac{\partial u_i}{\partial x_j} + \frac{\partial u_j}{\partial x_i}\right) - \frac{2}{3}\left(\frac{\partial u_k}{\partial x_k}\right)\delta_{ij}\right] \tag{4}$$

$$q_j = -\kappa \frac{\partial T}{\partial x_j} \tag{5}$$

and where μ is the dynamic viscosity, κ is the thermal conductivity, δ_{ij} is the Kronecker delta, ρ is density, and g is the gravitational acceleration. μ and κ depend on the temperature through Sutherland's Law (White, 1974). For the high frequency motions considered here the Coriolis force can be ignored.

The solution variables are ρ, the momentum per unit volume, ρu_i or (ρu, ρv, ρw), and the total energy $E = e + u_k u_k / 2 = c_v T + u_k u_k / 2$, with velocity components (u_i, u_j, u_k) along (x, y, z). Also $c_v = R/(\gamma - 1)$ is the specific heat at constant volume and T is the temperature. The compressible equation set is discretized using a second-order finite-volume scheme identical to the method discussed by Felten and Lund (2006). Our scheme is stable due to its kinetic energy-conserving construction and is therefore well suited for instability, transition, and turbulent flow regimes. This formulation results in exact numerical conservation of mass, momentum, and kinetic and thermal energy and thus faithfully represents the underlying conservation laws. Time advancement is achieved via a low-storage, third-order accurate Runge-Kutta scheme. Additional details for CGCAM are provided by Dong et al. (2020) and Lund et al. (2020).

3-D simulation cases discussed in this paper will make use of the dynamic Smagorinsky subgrid-scale model (Germano et al., 1991; Moin et al., 1991) to account for unresolved turbulent motions. The equations for the eddy viscosity, eddy conductivity, and turbulent kinetic energy coefficients are averaged over limited horizontal planes that contain just the turbulent flow. This is standard treatment and results in well-conditioned equations for the model coefficients (Germano et al., 1991; Moin et al., 1991).

2.2. CGCAM Configuration and Initial Conditions

Simulations are performed for a computational domain having dimensions $600 \times 600 \times 180$ km (x, y, and z) with resolutions of 0.4 km in each direction. Periodic boundary conditions are used at the lateral boundaries. An isothermal no-stress wall condition is used at the lower boundary, and a characteristic radiation condition is used at the upper boundary. The boundary conditions are supplemented with sponge layers at all streamwise and vertical boundaries to absorb outgoing GWs and AWs. The sponge layers are 20 km deep at the upper boundary, 5 km deep at the lower boundary, and 20 km wide on the streamwise and spanwise boundaries.

Our choices for GW parameters and the background state are made in part to enable reflection, trapping, and instability dynamics in the specified atmospheric profiles. The dispersion relation for GWs obtained from the linear Taylor-Goldstein equation provides valuable insights in studying GW dynamics, and can be written as

$$m^2 = \frac{N^2}{(c - U)^2} + \frac{d^2 U}{dz^2}\frac{1}{c - U} - \frac{dU}{dz}\frac{1}{H}\frac{1}{c - U} - \frac{1}{4H^2} - k^2 \tag{6}$$

where $U(z)$ is the mean horizontal velocity profile in the plane of wave propagation, H is the density scale height, $N(z)$ is the buoyancy frequency profile, k and m are the local GW horizontal and vertical wavenumbers, respectively, and c is the GW horizontal phase speed relative to the ground. In most cases of interest, the second and third terms in Equation 6 are small so that m^2 depends primarily on N, k and $c - U$. Equation 6 has GW solutions that are vertically propagating provided that $m^2 > 0$ and that are evanescent for $m^2 < 0$. Thus, GW trapping and ducting can occur for GW parameters and atmospheric profiles where $m^2 > 0$ only in certain height intervals. From the form of m^2 given by Equation 6, for sufficiently small k, this will occur for altitudes in the region where
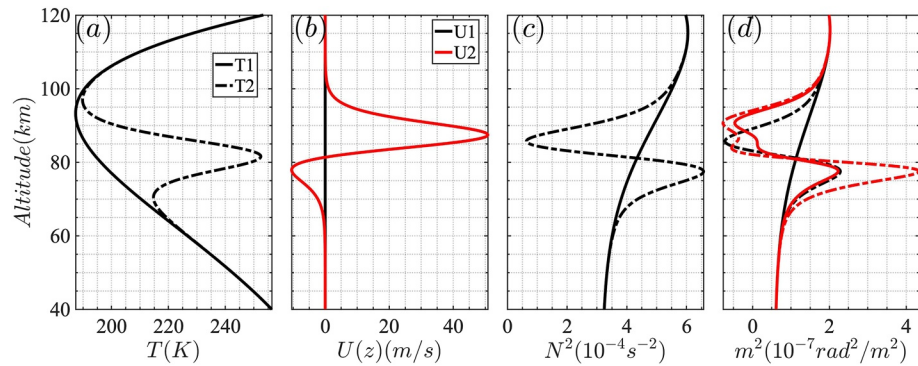
Figure 1. (a–d) $T(z)$, $N(z)$, $U(z)$ and $m^2(z)$ profiles for the mesospheric inversion layer (MIL) and tidal wind (TW) simulations: no MIL (solid black line), with MIL (dash-dotted black line), and TW (red lines).

either a maximum in N^2 occurs and/or a minimum in $c - U$ occurs (a velocity maximum in the direction of GW propagation).

We assume a nominal background temperature with $T_0(z) = 300\ K$ at lower altitudes, transitioning to a linear decrease with altitude and achieving a $-1.5\ K/km$ lapse rate by about 80 km altitude. $T_0(z)$ without the MIL is prescribed as

$$T_1(z) = \left\{ 1{,}000 + 700 \left[\frac{1}{2} \left(1 - \tanh \left(\frac{z - 120}{20} \right) \right) \right]^{0.2} \right\} \left[1 - 0.4\mathrm{sech} \left(\frac{z - 100}{55} \right)^2 \right] \tag{7}$$

This temperature profile has a minimum value of $\sim 187\ K$ at $\sim 95\ km$ altitude and increases to $\sim 255\ K$ at 120 km altitude.

In order to quantify the effects of a MIL and/or TW on GW evolutions we consider three different initial background temperature and wind environments. The first comprises the nominal temperature profile with no winds; the second comprises the nominal plus MIL temperature profile (see below) with no winds; the third comprises the nominal temperature profile with TW included; and the fourth comprises the nominal plus MIL temperature profile with TW included. The MIL structure is specified as

$$T_2(z) = T_0(z) \left\{ 1 + \beta \left[\frac{1}{\cosh \left(-\dfrac{z - z_{\mathrm{mil}}}{h_{\mathrm{mil}}} \right)} \right]^2 \right\} \tag{8}$$

Here $\beta = 0.3$ determines the degree of departure of the MIL from the nominal background temperature defined by Equation 8, $z_{\mathrm{mil}} = 82\ km$ is the center of the MIL structure, and $h_{\mathrm{mil}} = 6\ km$ determines the vertical scale of the MIL structure. To quantify the effects of TW on the GW evolutions and make a comparison with the MIL cases, we define a wind profile that provides a similar m^2 profile to the MIL case. For given values of c and k, this was achieved by substituting the value of m^2 from the MIL case with the nominal value of N into Equation 8 to derive U, see the red line (U2) in Figure 1b For all cases, an additional constant initial mean wind (22 m/s, not shown in Figure 1) opposite to the GW propagation is applied such that linear GWs evolve only in altitude and time.

We assume a GW packet propagating in the (x, z) plane having a Gaussian horizontal velocity (u' along x) amplitude of the form

$$u'(x, y, z, t) = u_0 e^{-\frac{(x - x_0)^2}{2\sigma_x^2} - \frac{(y - y_0)^2}{2\sigma_y^2} - \frac{(z - z_0)^2}{2\sigma_z^2}} \sin(k_0 x + m_0 z - \omega_i t) \tag{9}$$

Here $x_0 = y_0 = 0\ km$ and $z_0 = 40\ km$ are the initial central positions of GW packet in x, y, and z, respectively, and $\sigma_y = \sigma_x = 30\ km$, and $\sigma_z = 10\ km$ are the half widths of the GW packet in x, y, and z, respectively. Also, $k_0 = 2\pi / \lambda_{x0}$ and $m_0 = 2\pi / \lambda_{z0}$ are the horizontal and vertical wavenumbers, respectively, and $\omega_i = k(c - U)$ is the

Table 1
GW Parameters for Each Case Performed

| Case	λ_{x0} (km)	λ_{z0} (km)	u_0 (m/s)	Initial mean atmospheric state	2-D/3-D
1a	20	20	0.006	Only MIL (T_2, U_1)	2-D
1b	20	20	0.1	No MIL, No TW (T_1, U_1)	3-D
1c	20	20	0.1	Only MIL (T_2, U_1)	3-D
2a	20	20	0.006	Only TW (T_1, U_2)	2-D
2b	20	20	0.1	Only TW (T_1, U_2)	3-D
3a	20	20	0.006	MIL and TW (T_2, U_2)	2-D
3b	20	20	0.1	MIL and TW (T_2, U_2)	3-D

intrinsic frequency. The entire visible widths of the packet are about ∼180 and ∼60 km in the horizontal and vertical directions, respectively. The other perturbation quantities (spanwise velocity v' along y, vertical velocity w', temperature perturbation T', and density perturbation ρ') are then related to u' using the GW polarization relations following Dong et al. (2020). The GW and model parameters for each case are listed in Table 1. The horizontal intrinsic phase speed, $c_i = (c - U) = -44.4$ m/s, results in an intrinsic GW period of 450 s. Cases 1a, 2a, and 3a are used to examine the relative evolutions of a GW packet having a very small amplitude encountering MIL, TW, and MIL + TW, respectively. The other cases are used to explore a GW packet, with sufficient amplitude that could lead to nonlinear dynamics and potential instability, encountering MIL, TW, and MIL + TW.

3. Results and Analysis

3.1. Small-Amplitude GW Evolutions

Three cases (Cases 1a, 2a, and 3a in Table 1) are performed to illustrate the differences between small-amplitude GW packet evolutions in the MIL, TW, and the combined MIL and TW environments. Since there is no essential difference between GW evolutions under 2-D and 3-D conditions before they become nonlinear (e.g., Dong et al., 2020; F20), these simulations for small-amplitude GWs are only performed in 2-D. These three cases are compared by showing temporal evolutions of x-z cross sections of $\sqrt{\rho(z)/\rho_0}w'$ at $t = 35, 55, 75$, and 120 min in Figure 2. Considering Case 1a first (top row in the figure), by 35 min, the GW packet has entered the MIL region and the GW phase exhibits significant refraction. By 55 min, the GW packet exhibits partial downward reflection where $m^2 < 0$, partial GW packet transmission through the MIL, and partial trapping and horizontal propagation within the MIL.

Examination of Figure 2 reveals both strong similarities and clear differences between the three cases. Similarities include the following: (S1) Strong reflection and effective trapping, and (S2) similar dynamical time scales for reflection and transmission. Differences include the following: (D1) reduced transmitted GW amplitudes for stronger ducts in Case 3a, which are those with larger m^2 at the duct centers. (D2) larger horizontal velocities for the trapped GWs in the ducts when TW are included, and (D3) different morphologies of the trapped GWs. For
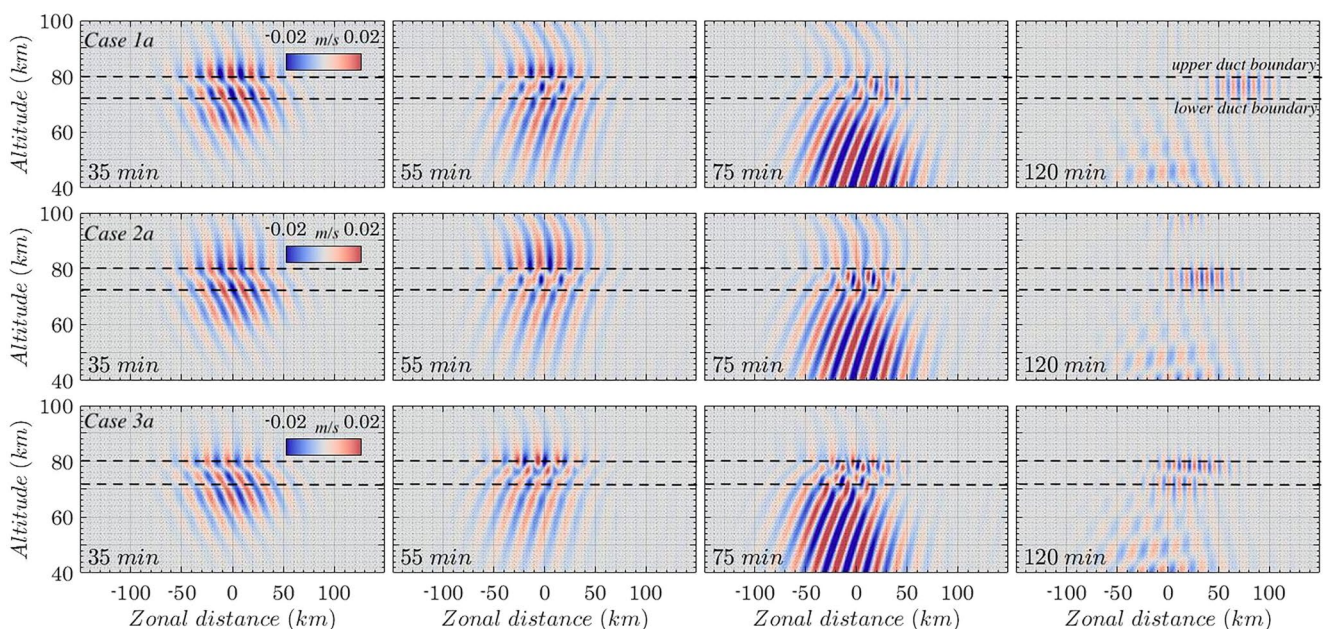
Figure 2. 2-D gravity wave $\sqrt{\rho(z)/\rho_0}w'$ x-z cross-sections at $t = 35, 55, 75$, and 120 min for Cases 1a (top row), 2a (middle row), and 3a (bottom row).

Case 3a, the trapped wave is attributed to the first mode because there is one node within the duct, while for Cases 1a and 2a, the trapped GWs are the zero mode because there is no node within the duct. A node occurs where $\sqrt{\rho(z)/\rho_0}\,w' = 0$ within the duct.

Similarities between the three cases are not surprising. The strong reflection and effective trapping arise due to the implications of Equation 5 for m^2, which suggests that the background conditions in all cases provide a suitable ducting environment for the specified GWs as shown in Figure 1d. Similar dynamical time scales for reflection and transmission occur because the GWs in these three cases have the same altitudes of reflection.

Differences noted above can also be traced to specific causes. Reduced transmission of GWs for stronger ducts is due to stronger reflection for incident GWs leading to increased trapping of spectral components within the ducts. A duct having regions of strong evanescence (negative m^2) extending over larger altitude ranges will allow more GW spectral components to exhibit ducting. A good example of this is shown by the dashed red line (MIL + TW) in Figure 1d. The strong dependence of c of the trapped GWs on U enables GWs having larger horizontal velocity to be trapped within the ducts including TW relative to those without TW; see Equation 5 and the discussion above. Referring to Figure 2, the λ_x in the three cases are ~10 km, which is half that of the primary GW packet and is the second harmonic arising from the initial GW packet (see the later discussion of the spectral results in Section 3.3). Previous studies (e.g., Dong, Fritts, et al., 2021; Dong, Hickey, & Zhang, 2021; Dong et al., 2018) have confirmed that the trapped GWs at the duct center should satisfy the relationship of $\lambda_z = 2h/n$, ($n = 1, 2$, and 3 are referred to as zero, first, and second wave modes, respectively), where λ_z are the vertical wavelengths of the trapped GWs, and h is the duct width. It can be seen from Figure 2 that most of the trapped GWs in Cases 1a, 2a, and 3a are confined to an ~20 km vertical region. Thus, the duct widths h should be ~20 km. According to $\lambda_z = 2h/n$, λ_z of the trapped GWs at the duct center are ~40, ~40, and ~20 km for Cases 1a, 2a, and 3a, respectively. Inspection of the spectral results for the $\sqrt{\rho(z)/\rho_0}\,w'$ over the t-x (temporal – zonal distance) domain and at the duct center confirm our derivations.

3.2. Large-Amplitude GW Evolutions

Figure 3 shows show x-z and y-z cross sections of u' at times of 20, 40, 60, and 80 min, while Figures 4 and 5 show x-y cross sections of u' at $z = 76$ and 110 km, respectively, at times of 20 (30 for $z = 110$ km), 40, 60, and 80 min. We begin with an overview of the major features of the GW evolutions in the absence of ducts. The evolutions of 2-D and 3-D large-amplitude GW packets were described in detail by Dong et al. (2020) and F20.

Cases 1c, 2b, and 3b address the same GW packets, but in different ducting environments (e.g., only MIL for case 1c, only TW for case 2b, MIL and TW for case 3b). Referring to Figure 3, at $t = 20$ min, the GW packets are still propagating upward and relatively weak in the mesosphere, but the GW packets above ~80 km exhibit clear phase refraction. At $t = 40$ min, there are clear modulations of the primary GWs by the ducts. The ducts cause partial trapping, reflection, and transmission of the GWs in the ducts from ~60 – 90 km. The transmitted GWs have propagated to higher altitudes and exhibited various dynamics spanning these times. The transmitted GWs in Cases 1c and 2b exhibit strong phase kinking, however, the stronger duct in Case 3b yields more effective trapping, and thus, the transmitted GWs in Case 3b still remain linear due to their reduced amplitudes.

For Case 1b without the ducting environments, the GW packet exhibits initial SA instability near 100 km. In contrast, the GW packets in Cases 1c, 2b, and 3b exhibit initial SA instability within the ducts. These dynamics are similar in form to those shown in F18 for a 1-D GW packet, and both reveal that (a) instabilities occur within the ducts when the GW amplitude approaches that required for breaking due to compression of the vertical wavelength accompanying the increasing m^2, and (b) ducts can cause large-amplitude GWs to yield instability below the altitude where they would otherwise arise. For the same GW packets, the altitude of instability generated by GWs in the presence of ducts is lower than that without ducts. For example, it can be seen in Figure 3 that the initial instability of Case 1b occurred at $z = $ ~100 km, which is higher than that of $z = $ ~80 km for Cases 1c, 2b, and 3b. The localization of 3-D GW packets also implies momentum transport that varies in x and z, acts as sources for larger-scale SGWs, and does not occur for 1-D GW packets.

By $t = 60$ min, the transmitted GWs in Cases 1c, 2b, and 3b exhibit similar dynamics to the primary GW in Case 1b, including strong SA instabilities, breaking, and SGW generation at higher altitudes (see Figure 3). In each duct case, some components of the primary GW packet are transmitted, reach altitudes above that of primary SA
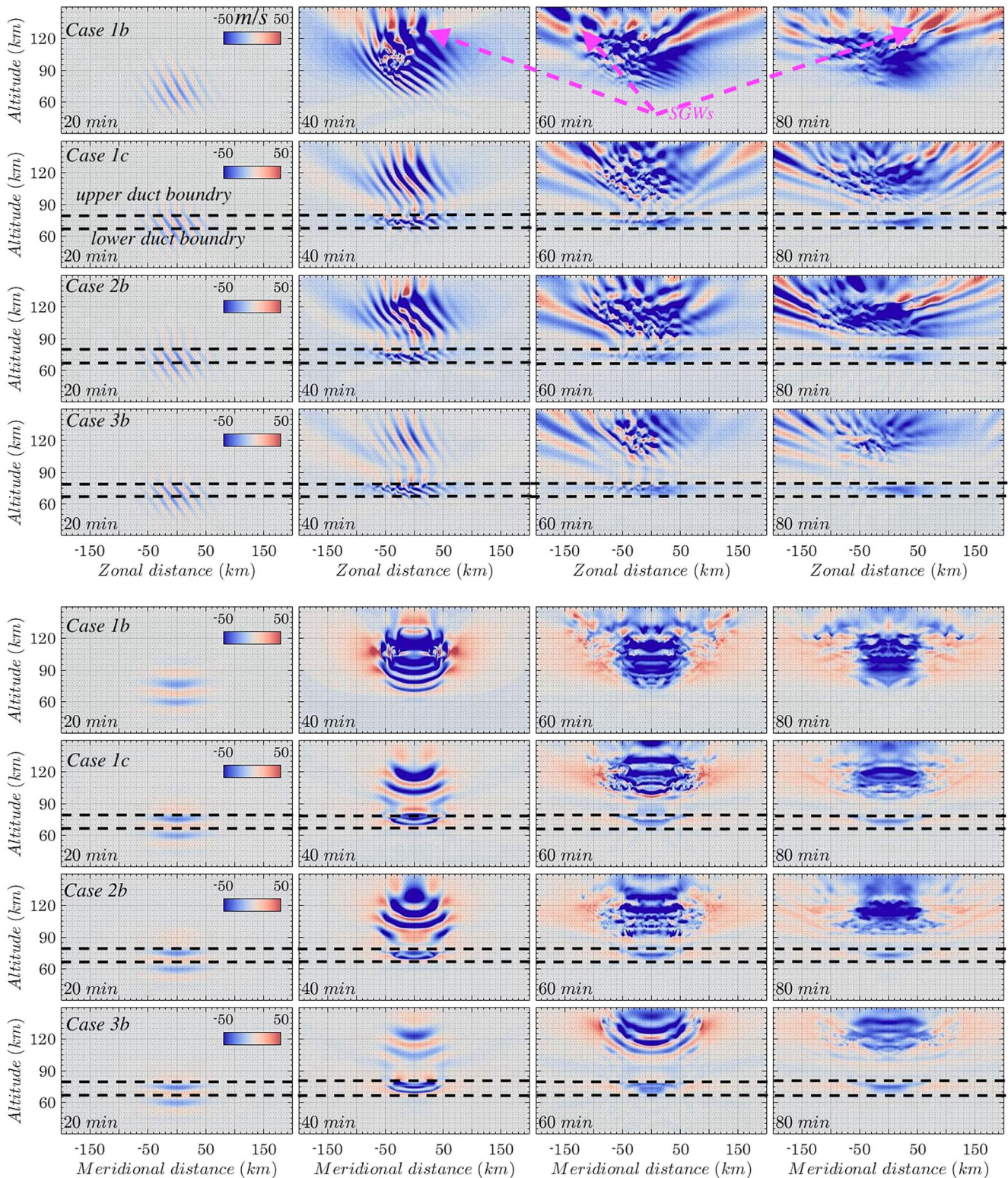
Figure 3. 3-D gravity wave u' x-z (y-z) cross-sections in the top (bottom) subpanels at t = 20, 40, 60, and 80 min for Cases 1b, 1c, 2b, and 3b, respectively (top to bottom in each subpanel).
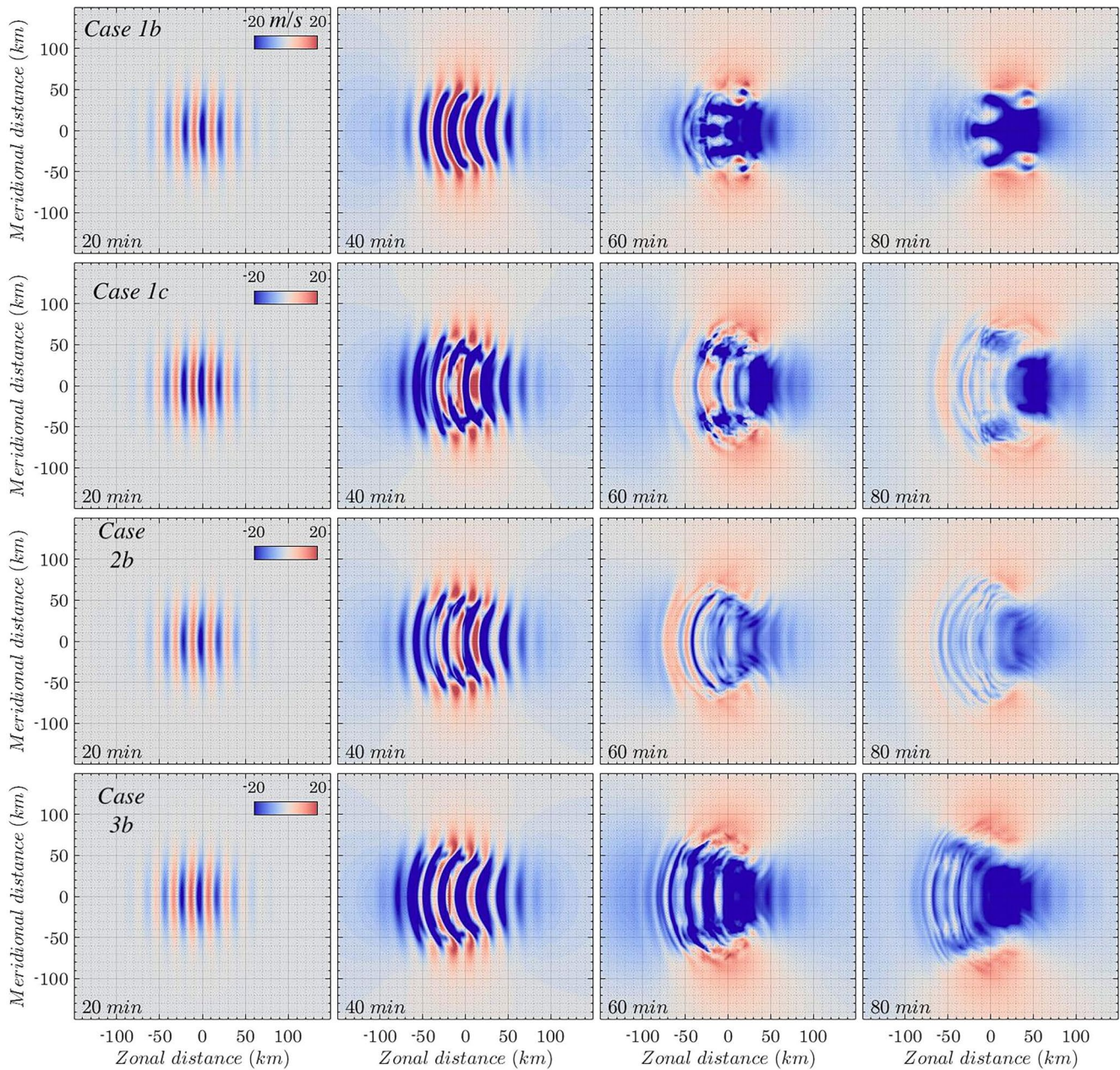
Figure 4. 3-D gravity wave u' x-y cross-sections at $z = 76$ km and $t = 20$, 40, 60, and 80 min (left to right) for Cases 1b, 1c, 2b, and 3b, respectively (top to bottom).

instability within the ducts, and continue to propagate to higher altitudes and induce SA dynamics, breaking, and SGW generation.

Beyond 60 min, instabilities that arose for transmitted GWs in all cases expanded spatially and decreased rapidly over time. In those cases, instabilities within the ducts dissipated rapidly, pseudo-momentum deposition induced mean flows within the ducts, and trapped GWs propagated horizontally and experienced a slight decrease in amplitude (see Figure 4).

Referring to Figures 3–5, we see both strong similarities and interesting differences among the GW dynamics in Cases 1c, 2b, and 3b. Similarities include the following: (S1) formation of strong layering due to the modulations by ducting environments; (S2) rapid cessation of transmitted GWs, and intense generation of SGWs following
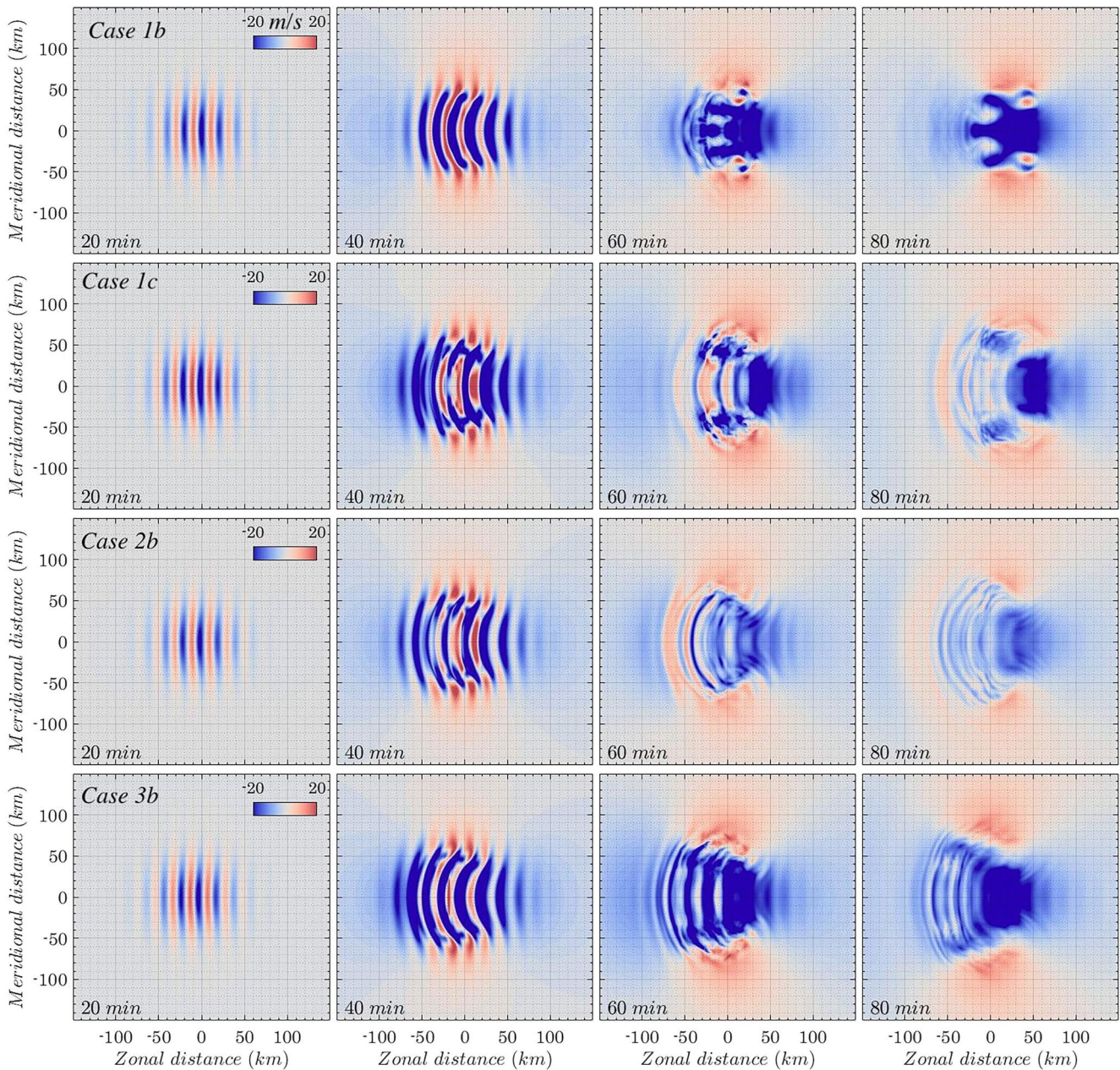
Figure 5. Same as Figure 4 for *x-y* cross sections at *z* = 110 km and *t* = 30, 40, 60, and 80 min.

initial instabilities; (S3) large GW amplitudes and ducting conditions lead to the initial instabilities within the ducts; and (S4) similar forms of trapped GWs arise within the ducts.

Differences among these results include the following: (D1) larger (smaller) amplitudes of trapped (transmitted) GWs in Case 3b due to its stronger ducting environment (See Figures 3 and 4); and (D2) the horizontal velocities of trapped GWs are largest (smallest) in Case 3b (Case 1c). As we discussed in Section 3.1 for these small amplitude GWs, U in the GW direction of propagation significantly influences c of the trapped GWs.

Summarizing, ducts can strongly modulate SGWs that arise from transmitted GWs by reducing their amplitudes to varying degrees, depending on ducting strength. Ducts also intensify GW amplitudes as the GWs approach ducts (compare the GW amplitudes between Case 1b without a duct and Cases 1c, 2 and 3b with a duct at *z* = ∼70–80 km in Figure 3), Cases 1c, 2b, and 3b with a duct induces GW trapping and smaller vertical
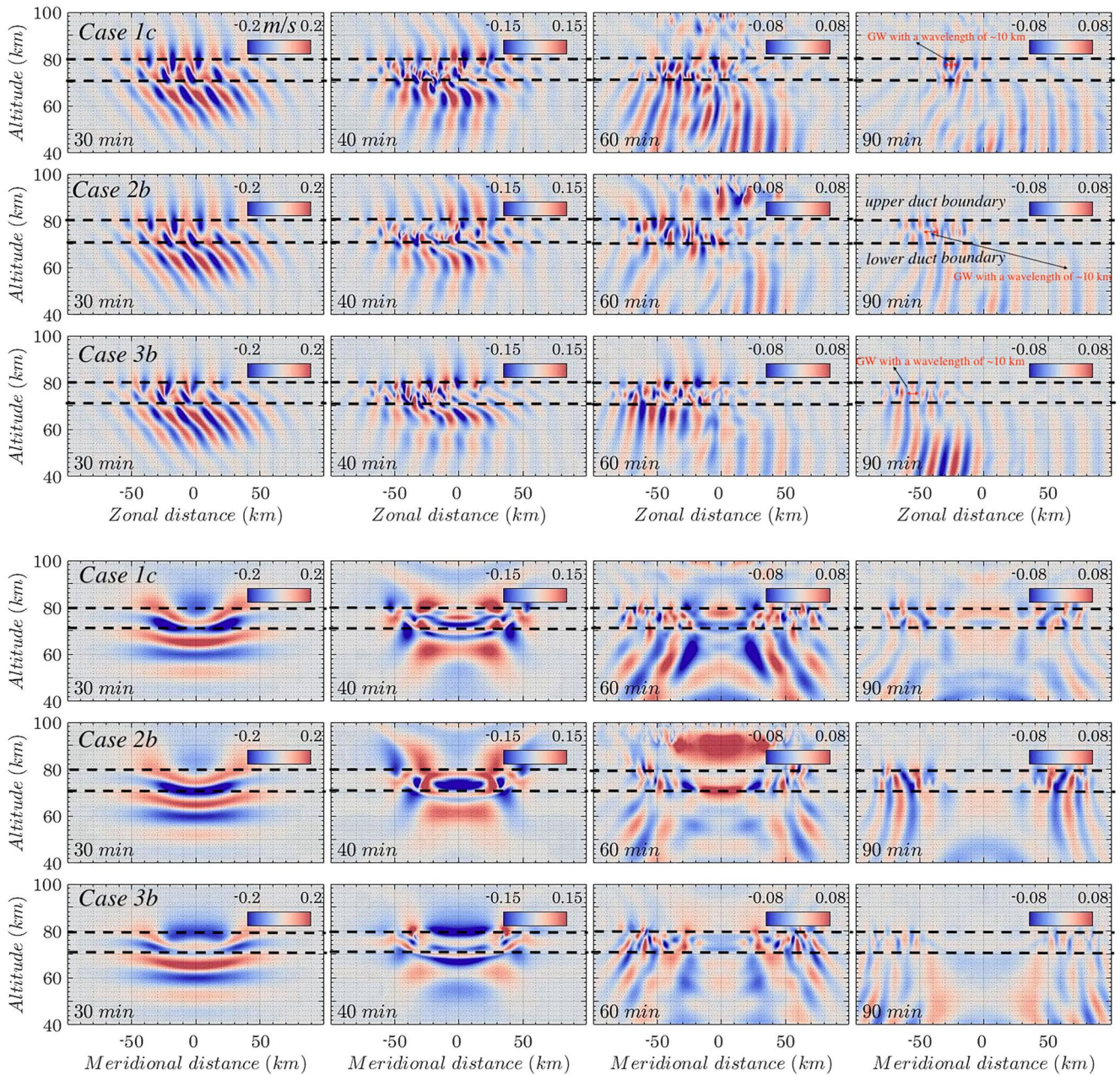
Figure 6. 3-D gravity wave $\sqrt{\rho(z)/\rho_0}w'$ x-z cross-sections (top subpanel) and y-z cross-sections (bottom subpanel) at t = 30, 40, 60, and 90 min for Cases 1c, 2b, and 3b (top to bottom at each subpanel).

wavelength (smaller m^2, see Figure 1d), hence exhibit the formation of shears that can enable instabilities, and reduced transmission and reflection.

We now explore the detailed dynamics of trapped GWs within the ducts for Cases 1c, 2b, and 3b. These are shown in Figure 6 with x-z and y-z cross sections of $\sqrt{\rho(z)/\rho_0}w'$ at times of 30, 40, 60, and 90 min. All exhibit strong instabilities within the ducts by t = 40 min. By t = 60 min, most of the instabilities have dissipated, with pseudo-momentum deposition accelerating the local mean flow. Interestingly, these responses include clear GWs having horizontal wavelengths of ~10 km within the ducts at this time that experience slight decreases in amplitude thereafter due to dispersion along the ducts and the energy leakages within the ducts.

The trapped GWs in Cases 1c and 2b are first modes, while for Cases 1a and 2a with the same configurations but with the smaller-amplitude GWs, the trapped GWs are zero modes. For Cases 1a and 2a, large-amplitude GW packets deposited momentum and energy within the ducts via breaking and dissipation, thus accelerated the mean flow along the GW propagation. The induced flow enhances the ducting environments, and the enhanced ducts have the potential to capture the spectral components with larger m^2.

It is worth noting that the source of those clear GWs that emerged above and below the ducts where the initial instabilities occur must be partially (or totally) due to GW reflection and transmission. However, instabilities dynamics within the ducts might contribute to these clear GWs by radiating SGWs to higher and lower altitudes that have both upstream (upward to the left) and downstream (upward to the right) phase alignments above the ducts. Previous studies have suggested GWs can be emitted from small-scale Kelvin Helmholtz instabilities (KHI), or localized KHI "packets", and from turbulent wakes (e.g., Abdilghanie & Diamessis, 2013; Bühler et al., 1999; Chimonas & Grant, 1984a, 1984b; Fritts, 1982, 1984). However, relative to the more widely recognized GW sources, these KHI sources have been much less studied to date.

3.3. Co-Spectral Evolutions

Spectra are useful to identify shifts in the dominant wavelengths as well as the onset of nonlinear transfers over a broad range of scales. In this section, we discuss the velocity and flux spectra, and how they reflect influences of modulations of ducting environments on GW propagation and spectral evolution. The 3-D simulation velocity spectra along the x and y directions, denoted $\langle u'^2 \rangle$ for $|x|$ and $|y| \leq 200$ km, are shown in the upper and lower panels in Figure 7, respectively. Perturbations are measured relative to instantaneous horizontal averages of the wind flow fields, that is $u'(x, y, z, t) = u'(x, y, z, t) - \overline{u}(x, y, z, t)$, where $\overline{u}(x, y, z, t)$ represents a horizontal average. The equivalent momentum and heat flux spectra, denoted $\langle u'w' \rangle$, $\langle v'w' \rangle$, $\langle w'T' \rangle$, are shown in Figure 8. The spectra are averaged over $|x|$ and $|y| \leq 200$ km, respectively, and averaged over 10-km altitude bins centered at 76 and 110 km, respectively. In order to clearly depict GW dynamics and energy transfers from the initial GWs to instabilities leading to turbulence, we show only the low wavenumber portion of each spectrum.

Considering first the spectra for Case 1b and referring to the first column in Figure 7, we see that $\langle u'^2(k) \rangle$ largely reflects the initial GW packet wavenumber dependence in k with the major peak at $\lambda_{x0} = 2\pi/k_0 = 20$ km and its second harmonic peak at $\lambda_{x1} = 2\pi/k_1 = 10$ km (see the gray lines at $t = 20$ min). At $t = 30$ min (blue lines), the GW packet has propagated $\sim$25 km higher, the amplitude of the GW and its second harmonic peak have further increased, initial SA instabilities have achieved large amplitudes, and initial SGWs have appeared above $z = 110$ km. These yield spectral slopes for k and l approaching $-5/3$ corresponding to $\sim$5–15 km wavelengths due to transfers of GW energy to small-scale instability structures, turbulence, and SGWs. At this time, the k and l spectral amplitudes are consistent, suggesting a relatively isotropic spectrum at $z = \sim$110 km as a result of strong instability dynamics spanning a broad region. GW packet instabilities and the generation of SGWs decrease significantly from $t = \sim$60 to $\sim$80 min. The spectra reflect these dynamics, where spectral amplitudes at $\sim$110 km for λ_x and $\lambda_y \sim 15$ km are smaller by factors of $\sim$10 or more at $t = 80$ min relative to those at $t = 40$ min.

The strong influences of ducts on the various GWs can be seen in the spectra. The k spectra for Cases 1c and 3b shown in columns 1 and four of Figure 7, respectively, agree closely at $t = 20$ min and $z = \sim$76 km. This is because most of the initial GW packet still lies below the duct, so there is only weak refraction at the leading edge of the GW packet at this time.

By $t = 40$ min, differences between the different cases have increased at all altitudes. As discussed above, the ducts caused the initial GW instabilities and dissipation to occur within the ducts, which is below where they would otherwise occur. The 3-D spectra in Cases 1c, 2b, and 3b reflect these dynamics, where spectral slopes at $z = \sim$76 km for k and l corresponding to $\sim$5–15 km wavelengths approach $-5/3$ due to the conversion of GW energy into 3-D instabilities, turbulence, and high-frequency and small-scale SGWs that are emitted from instabilities.

By comparison, there is no $-5/3$ slope at $z = \sim$76 km in Case 1c in the absence of a duct. This is because there are no energy conversions from GWs to instabilities at $z = \sim$76 km in Case 1c at this time (see Figure 3). For Case 3b, the transmitted GWs have propagated to altitudes of $\sim$100 – 130 km and have similar parameters to the initial GW packet (e.g., horizontal wavelength) except for the amplitudes by $t = 40$ min. In response, the k spectra (blue line) at $\sim$110 km in the fourth column show similar transmitted GW packet wavenumber dependence in k
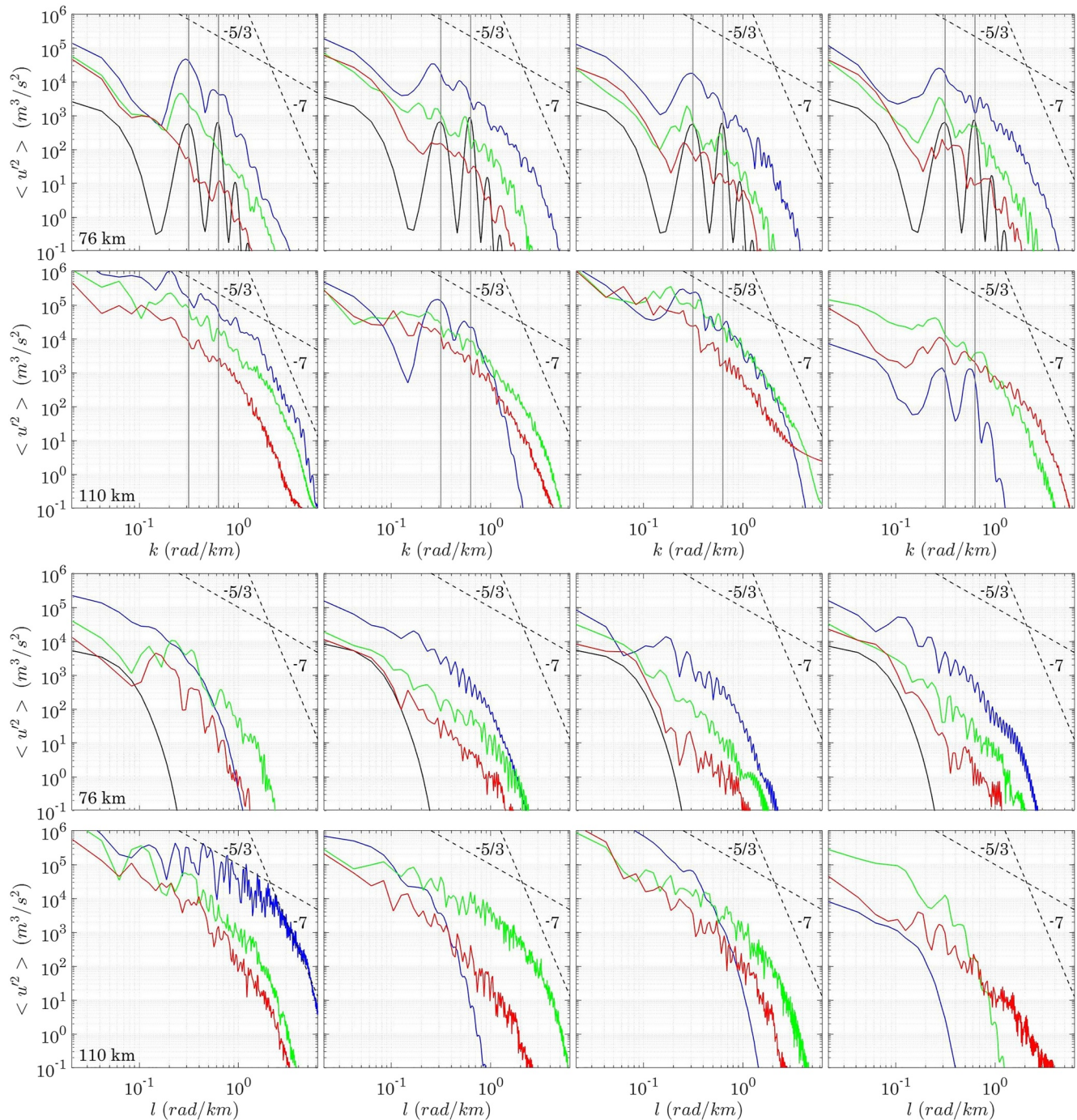
Figure 7. x Power spectra of u' averaged in the orthogonal direction and in 10-km altitude bins with centers at $z = 76$, and 110 km in Case 1b (first column), Case 1c (second column), Case 2b (third column), and Case 3b (fourth column). Times of 20, 40, 60, and 80 min are shown in black, blue, green, and red. The $-5/3$ and -7 slopes are shown as dashed black lines at upper right and the spectral range extends from 1 to 400 km in each panel. The gray lines denote the first ($\lambda_x = 20$ km) and the second ($\lambda_x = 10$ km) harmonics of the initial GW packet, respectively.

(the major peak and its second harmonic peak) to that of the initial GW packet, as expected from inspection of Figure 3. At later times, a $-5/3$ spectral slope is expected for the transmitted GWs, given that they are dictated by the character of the underlying GW field.

The spectra associated with GW evolutions for the varying ducting environments defined by Cases 1c, 2b, and 3b are shown in columns 2, 3, and four of Figure 7, respectively. Strong similarities and clear differences amongst
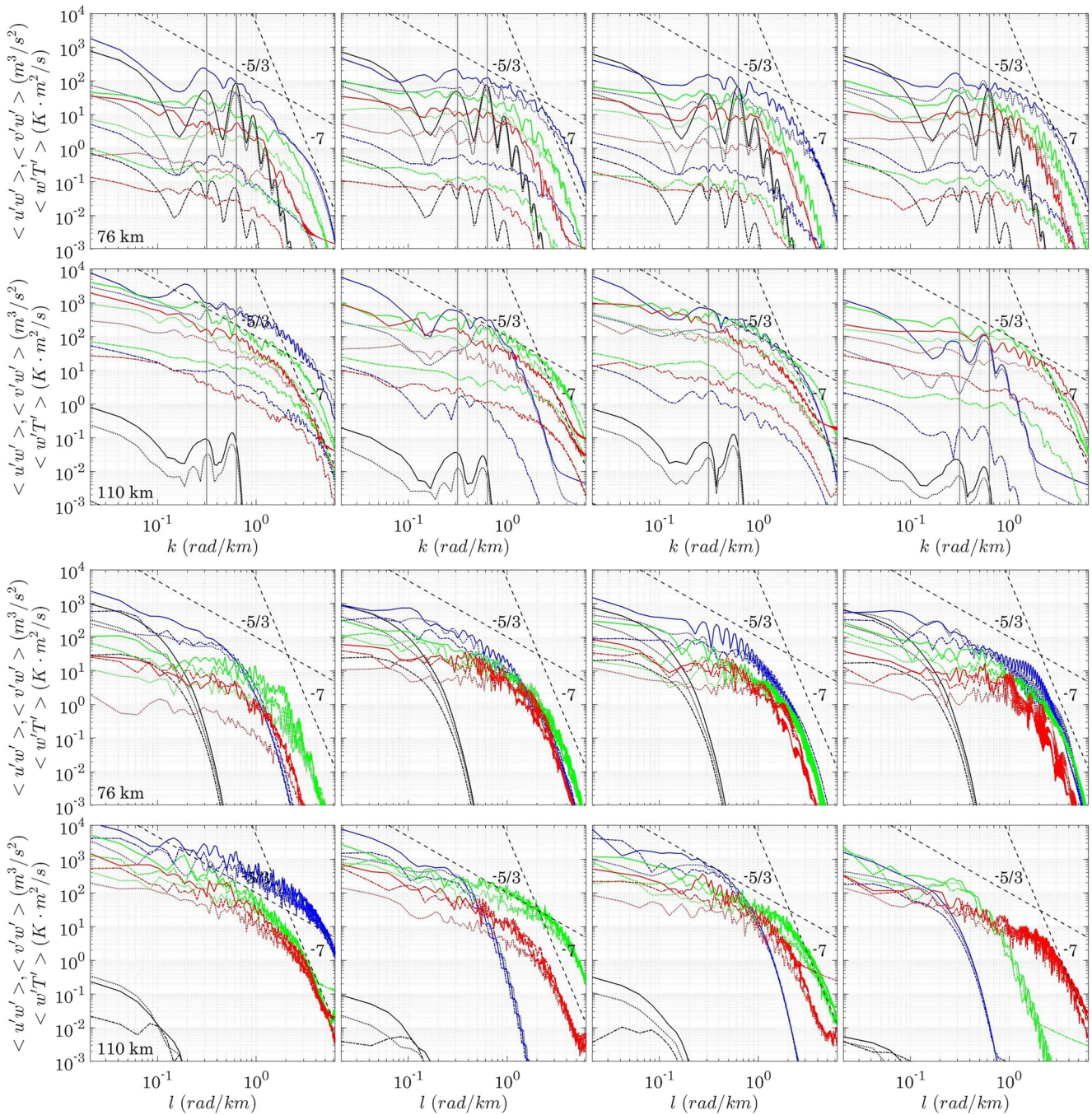
Figure 8. As in Figure 7 for the $\langle u'w' \rangle$, $\langle v'w' \rangle$, and $\langle w'T' \rangle$ cross spectra (solid, dashed, and dotted lines, respectively) along x and y. Units for the three cross spectra are m³/s² and $K \cdot m^2/s$.

the three cases can be seen. Similarities include the following: (S1) nearly identical spectral evolutions at duct altitudes, such as the −5/3 and −7 spectral slopes; (S2) for the transmitted GWs, the three cases exhibit a dependence on the wavenumber k at early times, and the related dynamics yield a −5/3 spectral slopes at later times. Differences include the following: (D1) the spectral amplitudes at 110 km altitude are smaller by factors of ∼5–25 times or more for the stronger ducting environments relative to the weaker ducting environments (see the red lines in second and fourth rows in Figure 7).

For the flux spectra shown in Figure 8, we again see the spectral responses to modulations of the ducting environments on GW evolutions. For the spectra at $t = 20$ min (black lines), the major fluxes accompany the initial GW and its harmonics. Of these, the first and second harmonics make the major contributions at ducting altitudes ($\sim$76 km) to $u'w'$, $v'w'$, and $w'T'$. Furthermore, the amplitudes of the second harmonic are slightly larger than those of the first harmonic. By $t = 40$ min, differences between the spectra with and without ducting environments are seen to increase at ducting altitudes. For the spectra with ducts, the cascade of energy to smaller scales in regions of active GW instabilities in the ducts yields the spectral slopes of $-5/3$ at scales of $\sim$5–10 km. This is not seen in the spectral results without ducts due to the GW breaking occurring above $z = \sim$80 km. More dramatic differences are seen at $z = \sim$110 km, where the ducting modulations yield reduced spectral amplitudes and a delayed formation of $-5/3$ spectral slopes due to the reasons discussed above. At later times, comparable spectral amplitudes in k and l indicate relatively isotropic spectra at ducting altitudes and the altitudes where the transmitted GW breaking occurs.

3.4. GW Energy, Momentum Flux, and Induced Mean Flow Evolutions

3.4.1. GW Energy Evolutions

Figure 9 depicts the GW energy evolutions under varying background environments corresponding to Cases 1b, 1c, 2b, and 2c, respectively. The GW total energy, E' $\left(E' = \frac{1}{2} \left(u'^2 + v'^2 + w'^2 \right) + \frac{1}{2} \frac{g^2}{N^2} \frac{T'^2}{T_0^2} \right)$, is summed over $|x| \leq 200$ km for each altitude and shown in the top panel of Figure 9. The middle and bottom panels of Figure 9 show the summed E over altitude bins of 60–87 km and 87–150 km, respectively.

Without the ducting environments, the GW energy grows exponentially in altitude, approximately preserving its vertical profile as it penetrates to higher altitudes where it is dissipated. At $t = 30$ min (blue lines), the GW packet peak has propagated to $z = \sim$95 km where it has remained largely linear. By $t = 45$ min, smaller disturbances occurring in the energy profile indicate strong GW breaking and related dynamics at this time. Beyond 45 min, the GW energy experiences a rapid decrease due to GW dissipation driving energy and momentum deposition.

For Cases 1c, 2b and 3b having ducts, we see that E is largest below $\sim$90 km altitude and that most of the GW energy is constrained within the ducts at $t = 30$ min. By $t = 40$ min, the GW energy within the ducts experiences a slight decrease for three reasons, including (a) GW dissipation through the conversion of energy from GWs to instabilities and turbulence; (b) energy leakage from the ducts; and (c) radiation of high-frequency SGWs from instabilities within the ducts. At this time, the transmitted GWs have achieved breaking amplitudes in Cases 1c and 2b, but not yet in Case 3b.

For specified GW sources, a stronger duct implies that less GW energy will tunnel into the ducting region from outside the duct, and also less energy will leak from the ducting region. This can be seen in the middle panel of Figure 9, where the maximum energy entering the duct in Case 3b is less than that for Cases 1c and 2b. However, beyond $\sim$070 min, the trapped GWs for these three cases are nearly identical. The reason for this is that strong 3-D instabilities, contributing to the maximum energy within the duct, have dissipated and deposited energy into the mean flow after they emerged. Additionally, the long-lived, small-scale, trapped GWs with horizontal wavelengths $\sim$10 km, which arise from the second harmonic of the initial GW packet and/or initial GW packet breaking, become the main contributor to the trapped energy at later times. The bottom panel of Figure 9 shows, as expected based on the discussion above, that the transmitted GW energy in Case 3b is less than that in both Cases 1c and 2b.

3.4.2. GW Momentum Flux Evolutions

Figures 10 and 11 show the time-averaged momentum flux $\left(\sqrt{(u'w')^2 + (v'w')^2} \right)$ for Cases 1b, 1c, 2b, and 3b at $\sim$76 and 110 km altitudes, respectively. The momentum flux was averaged over 0–30, 30–60, and 60–90 min of the simulation.

Perturbation fields shown in Figures 3–5 and spectral evolutions shown in Figures 7 and 8 reveal the evolutions of the 3-D GW packet accompanying the exponentially increasing amplitudes. Additional responses in x and y arise due to propagation in the varying ducting environments imposed at $z = \sim$76 km. The ducting conditions act
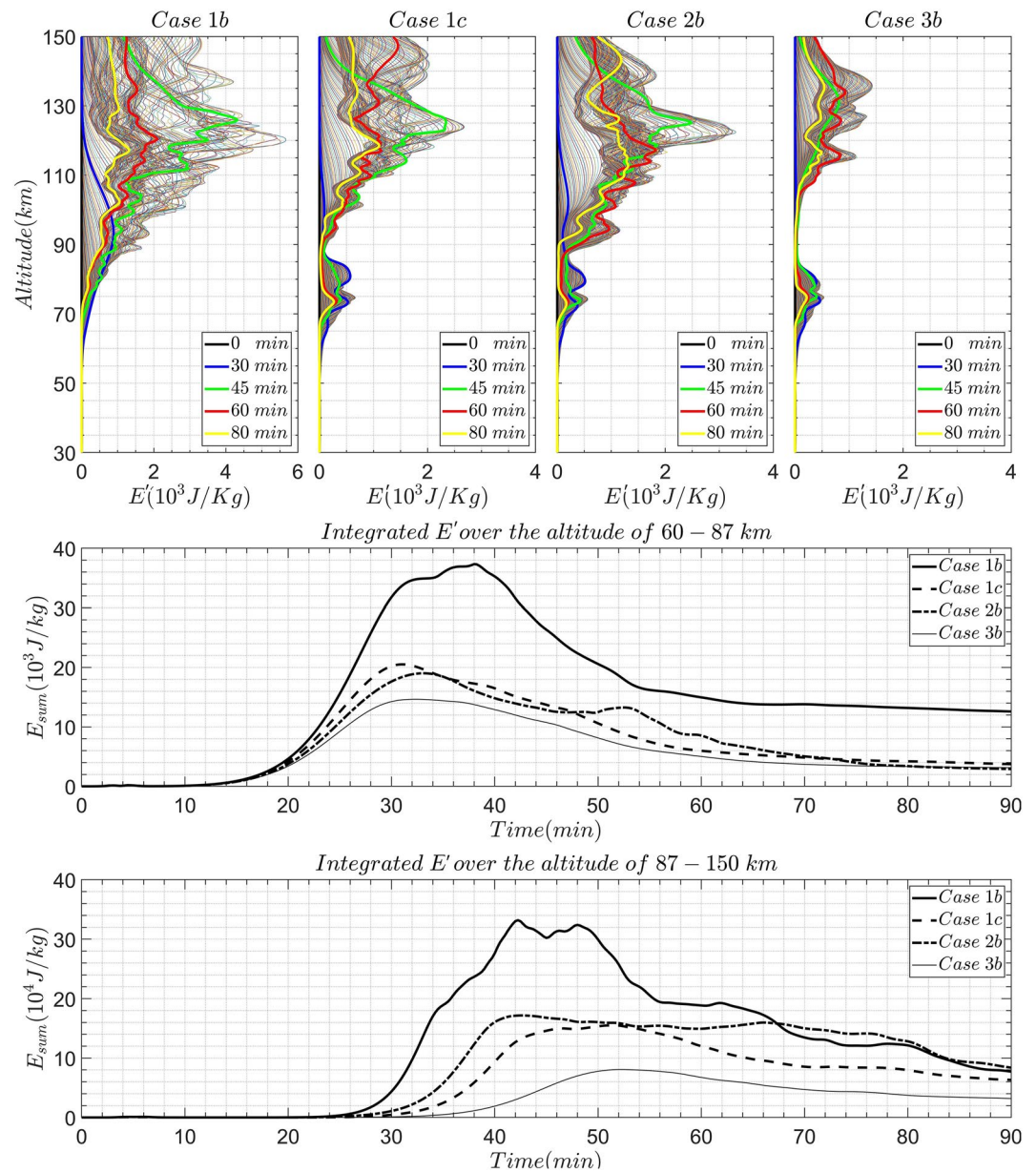
Figure 9. (top panel) Profiles of GW total energy, E, for Cases 1b, 1c, 2b, and 3b. The thin solid colored curves are the profiles at each simulation time step. The thick solid colored curves are the profiles at the time steps shown in each panel. (middle panel) Time series of integrated GW energy over 60–87 km. (bottom panel) Profiles of integrated GW energy over 87–150 km.

to dissipate GWs and decrease their fluxes for GWs experiencing decreasing phase speed $|c_i|$ and vertical wavelength λ_z, and to enable GWs having increasing $|c_i|$ to have increasing fluxes. The fluxes are thus highly structured within the ducting environments and they have different influences in different portions of the GW fields.

The flux fields shown in Figures 10 and 11 clearly reveal these dynamics. Considering the first-interval, the fluxes exhibit nearly identical characteristics at $z = \sim 76$ km, however, large differences are seen in their magnitudes at $z = \sim 110$ km. The reason for this is that only a small part of the leading edge of the initial 3-D GW packet is influenced by the ducting environments for times up to 30 min. After 60 min, increasing differences are seen at both $z = \sim 76$ and 110 km. At $z = 76$ km, the fluxes expand along the x and y directions and are mainly contributed by small-scale instabilities structure caused by GW breaking. At $z = 110$ km, the fluxes are associated with small-scale structures due to the breaking of transmitted GWs. The stronger ducting environment of Case
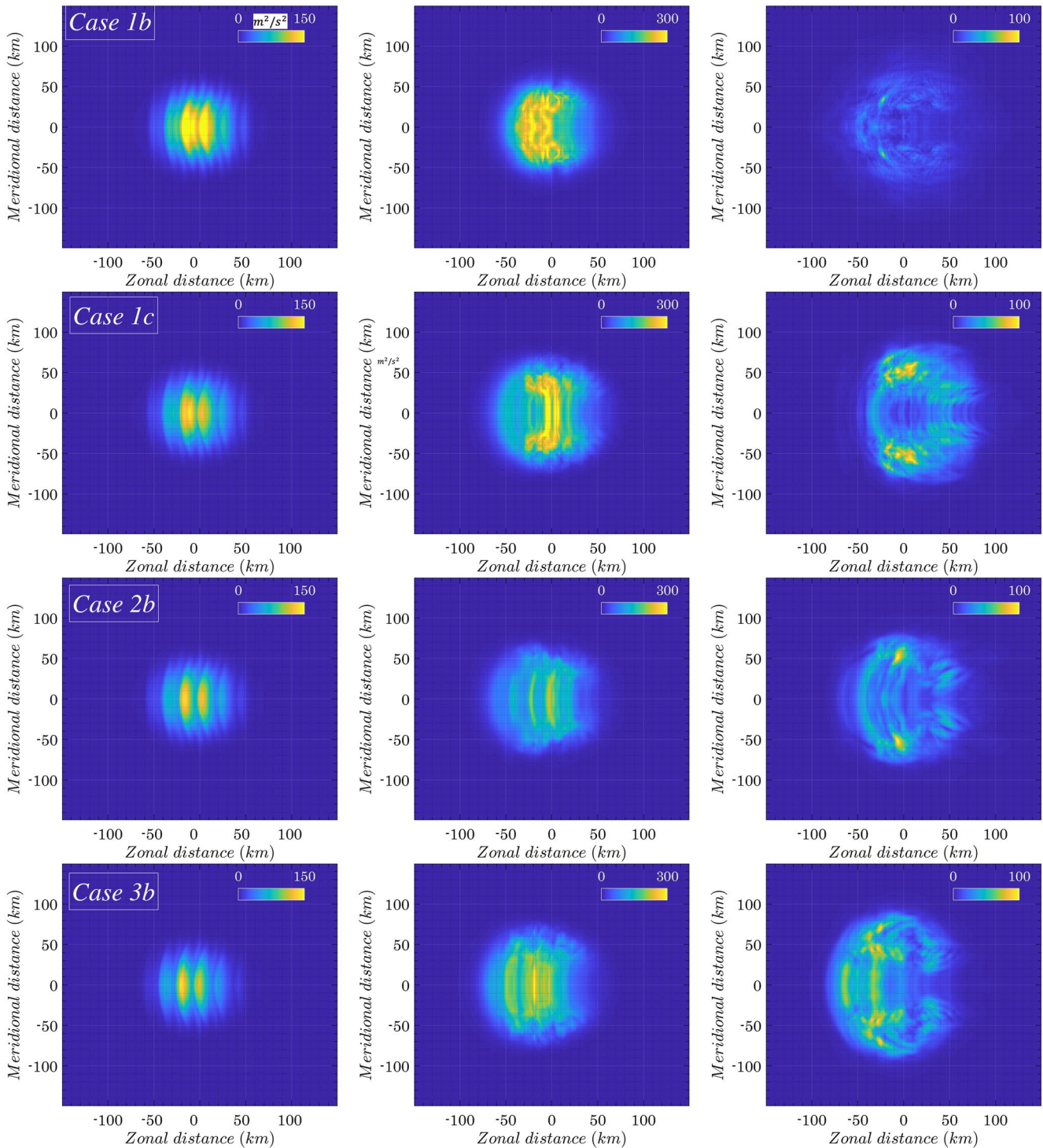
Figure 10. The time-averaged momentum flux $\left(\overline{\sqrt{(u'w')^2 + (v'w')^2}}\right)$ at $z = 76$ km for Case 1b (first row), 1c (second row), 2b (third row), and 3b (fourth row). The momentum flux averaged over (left) 0–30 min, (middle) 30–60 min, and (right) 60–90 min of the simulation.
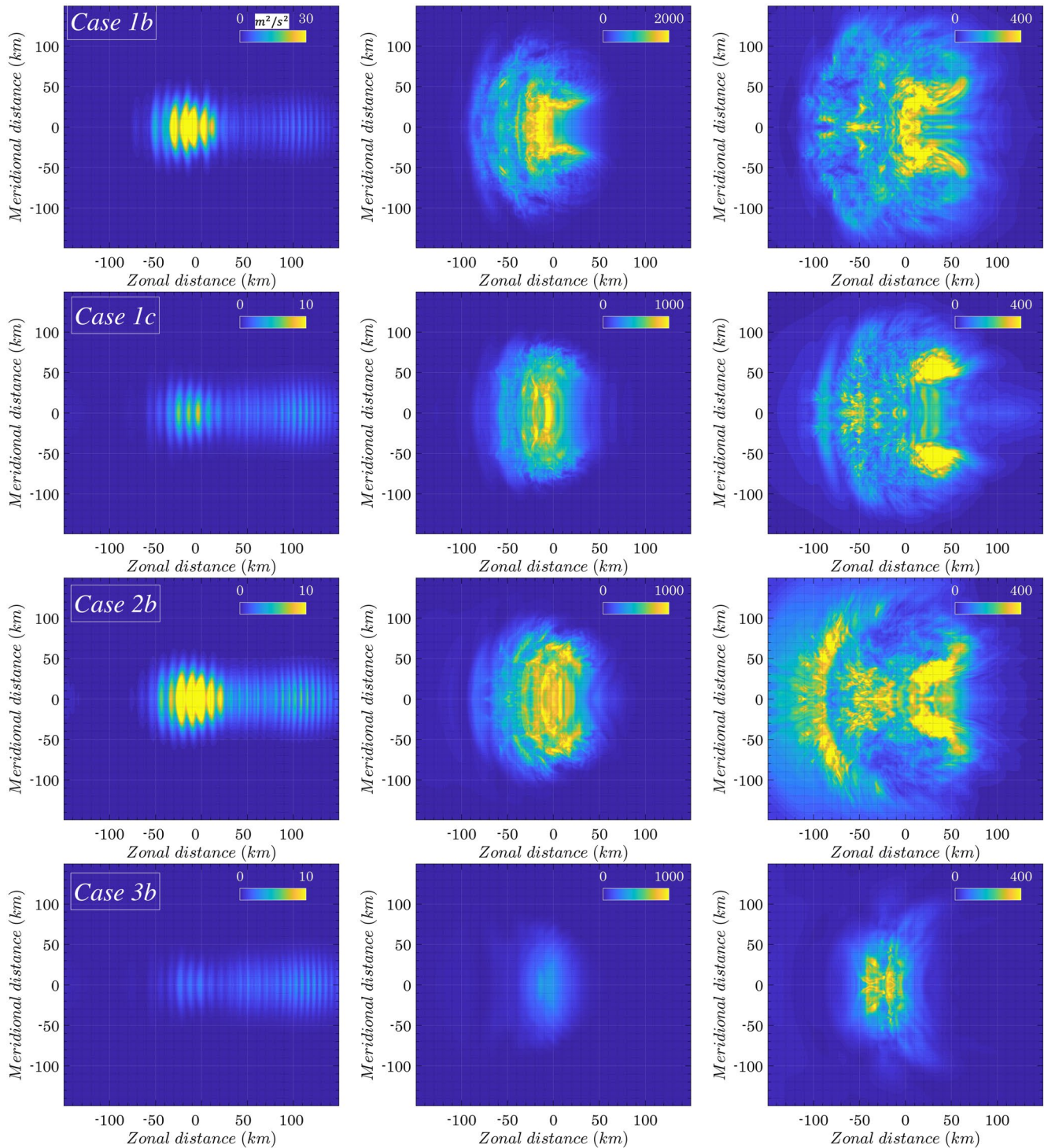
Figure 11. Same as Figure 10 for 110 km altitude. Note that the color scales for Case 1b are different from those in Cases 1c, 2b, and 3b.

3b blocks GW energy propagation to higher altitudes, thus yielding weaker local responses at 110 km than for the other cases.

After 90 min at $z = \sim 76$ km, the Case 1b fluxes have experienced a large decrease due to strong instability-driven dissipation, but Cases 1c, 2b, and 3b fluxes experience only slight decreases and retain the influences of the ducting modulations. The Case 3b fluxes have shifted toward negative x values with respect to the packet center
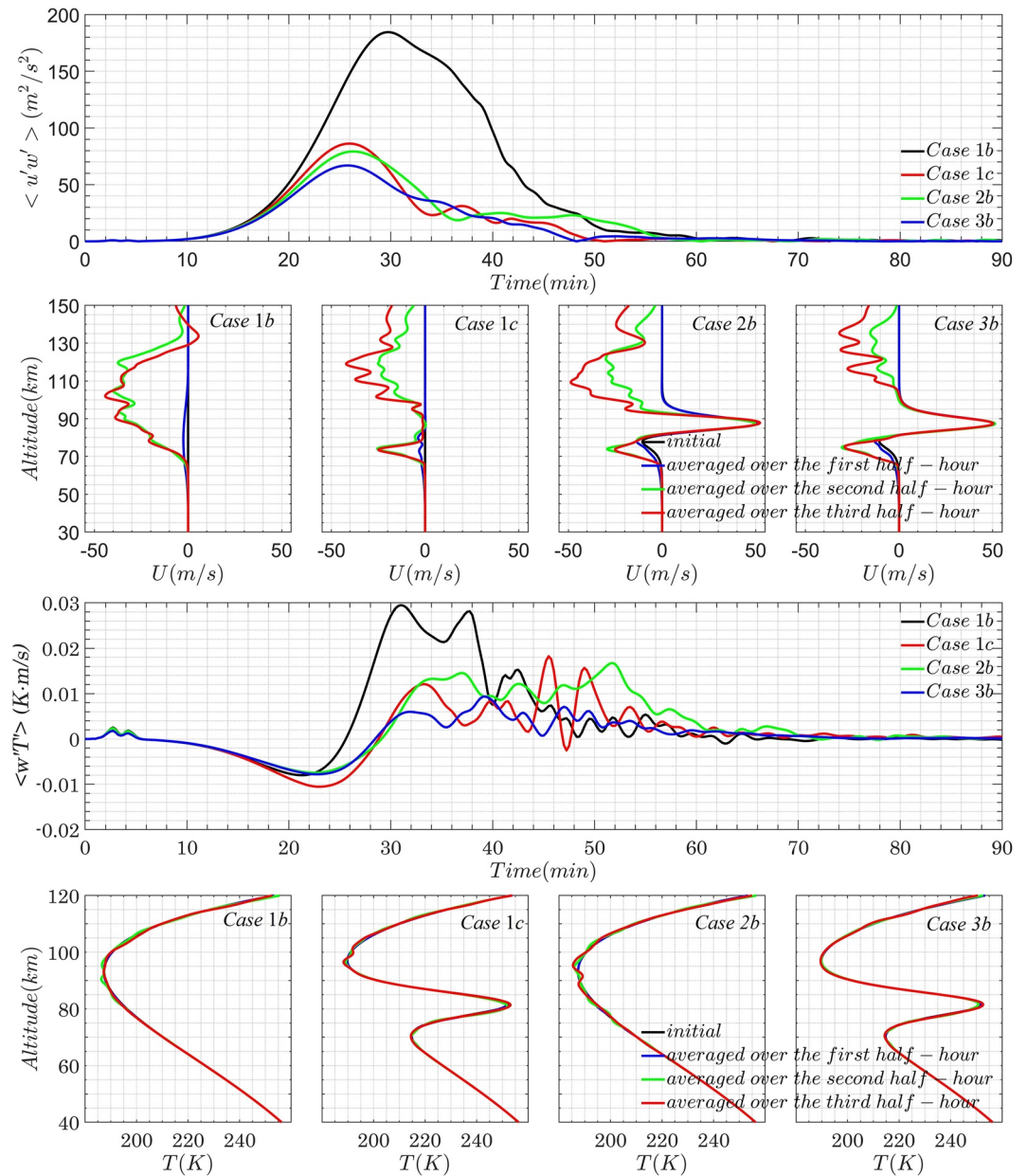
Figure 12. Gravity wave $\langle u'w' \rangle$ (first row) and $\langle w'T' \rangle$ (third row) as functions of time. They are obtained by averaged from $z = 60$–87 km. The second and fourth rows show the mean wind and temperature fields during the three intervals for Cases 1b, 1c, 2b, and 3b (left to right).

because of the stronger induced wind shear in the stronger ducting environment. As was seen for the transmitted fluxes at $z = \sim 110$ km during at 30–60 min, the Case 3b fluxes are largely constrained by the stronger ducting environments, and thus their influences on the mean flow are more local than in other cases.

3.4.3. GW Induced Wind and Thermal Structure Evolutions

The mean flow accelerations and heating are directly related to the momentum and heat fluxes, respectively. These fluxes may undergo significant changes because of GW breaking and resulting instabilities. In this section, we examine the momentum and heat fluxes, and their induced mean flow evolutions accompanying the GW breaking described above. Figure 12 shows the momentum and heat fluxes as functions of time. They are obtained by averaging $u'w'$ and $w'T'$ over the region exhibiting instabilities from $z = 60$–87 km. The mean wind $U(z)$ and temperature $T(z)$ fields during 30-min intervals of the simulation for Cases 1b, 1c, 2b and 2c are also shown in

Figure 12. The quantities $\triangle U(z)$ and $\triangle T(z)$ are calculated by averaging u' and T' over x between -60 and 60 km at each altitude and using a 30-min temporal window.

The momentum fluxes $\langle u'w' \rangle$ (top panel of Figure 12) and the quantity $U(z)$ (second row of Figure 12) increase with time until reaching their maximum values at times of ~ 26 and 30 min for the three ducting cases (Cases 1c, 2b, and 3b) and the no duct case (Case 1b), respectively. The increasing momentum fluxes beyond $t \sim 10$ min imply large momentum fluxes into the ducting environments, strong and transient momentum flux divergences, and strong local mean-flow accelerations prior to significant GW dissipation.

The maximum $\langle u'w' \rangle$ occurs between $t = \sim 20$ and 30 min prior to the generation of strong 3-D instabilities. Thus, the largest $\langle u'w' \rangle$ must be attributed to the 2-D GW and instability dynamics rather than to 3-D instabilities. The largest momentum flux in Case 1b is delayed due to the delayed formation of the initial 2-D SA instability dynamics. The $\langle u'w' \rangle$ in the ducts decrease from their maximum values that begin at $t = \sim 26$ and 30 min accompanying 2-D and 3-D instabilities in the ducting cases and Case 1b, respectively, thus increasing the $\langle u'w' \rangle$ convergence between the ducting level and the stable region below. This accelerates the mean flow and extends the shear layer to lower altitudes, which can be seen from the induced wind shear in the second row in Figure 12. The induced winds in the ducting region from 30 to 60 min are ~ 25, 30 and 30 m/s in Cases 1c, 2b, and 3b, respectively, and can survive to much later times despite the decreasing $\langle u'w' \rangle$.

Figure 12 also shows $\langle w'T' \rangle$ and the related temperature changes. The thermal structure in the ducting region remains almost unchanged throughout the simulation time, implying that cooling and warming terms closely balance each other, and net heating is negligible. The failure of GW breaking to induce an obvious change in the temperature field suggests that such GW-induced heating is not as strong as previously assumed.

4. Discussion

Employing high-resolution simulations, we have examined the dynamics of GWs encountering a highly structured wind and temperature environment. Modeling responses include GW transmission, reflection, SA and instability dynamics, SGWs generation, and the induced mean wind and temperature evolutions. Here we provide a more extensive discussion of the impacts of GW breaking on mean temperature profiles.

As expected, we see that momentum deposition in ducts due to GW breaking accelerates the mean flow along the GW propagation direction. However, the GW breaking process induced by a single wave packet of initially small amplitude at 40 km altitude does not yield significant net heating or cooling. Similar results were obtained by F18, who employed a high-resolution anelastic 2D numerical model to explore the dynamics of GWs entering a MIL. In their cases, they found that GW breaking does not cause the local mean thermal structure to approach an adiabatic lapse rate. This similarity indicates that heat flux and its divergence are insensitive to the differences in GW breaking process for 2D and 3D GW packets. These results suggest inefficient vertical heat fluxes due to GW breaking in line with the initial theoretical considerations by Fritts and Dunkerton (1985), Coy and Fritts (1988), and McIntyre (1989) suggesting an effective Prandtl number, $Pr \sim 2$ or greater, that appears to have been confirmed in initial and more recent global modeling (Garcia et al., 2017; Strobel et al., 1985, 1987), and in the modeling exploration of MIL dynamics by F18.

Nevertheless, it has been argued that GW breaking can affect the thermal structure due to GW amplitude growth with altitude and instabilities that occur for all GW amplitudes and intrinsic frequencies (e.g., Liu & Hagan, 1998; Liu et al., 1999, 2000), but these studies did not resolve the instabilities and turbulence driving the mean state evolution.

Observations from multiple lidar measurements suggest potentially significant vertical heat fluxes of 1–2 Km/s (Gardner & Liu, 2007; Gardner & Yang, 1998; Guo & Liu, 2021), significantly larger than in this model simulation. However, these estimates likely have significant uncertainties, as their implications for mean state evolutions are not consistent with the high-resolution modeling fully describing instability dynamics and their implications for mixing and heat transport reported here and cited above.

Various other mechanisms expected to influence the thermal structure of the atmosphere include the following:

1. Turbulent dissipation of GW kinetic energy yielding heating (e.g., Ebel, 1984);

2. Frictional heating converting GW kinetic energy to internal energy (heating) in a viscous atmosphere precluding turbulence generation(e.g., Medvedev & Klassen, 2003);

3. Divergence of the vertical heat flux causing local heating and cooling, but no net heating or cooling (e.g., Walterscheid, 1981); and

4. Exothermic chemical reactions, which can be altered by the presence of GWs and create local heating. For example, Meriwether and Mlynczak (1995) and Fadnavis and Beig (2004) have illustrated the importance of chemical heating in causing MILs between $z = 80$ and 90 km.

Our CGCAM simulations of GW heating/cooling effects directly include the first and second mechanisms listed above. The third mechanism, eddy diffusion, is implicitly included in the model and is large only when and where there is active GW breaking. This is different from those considered in studies such as Walterscheid (1981) and Liu et al. (2000) where an eddy diffusion coefficient is prescribed. Implied in these latter studies is a background eddy diffusion that acts to mix the local atmosphere, but in a manner that is apparently not consistent with our direct modeling of the underlying dynamics including instabilities, turbulence, and their mean state influences. The fourth mechanism, exothermic chemical reactions, is dependent on the densities and temperature of reacting species and can certainly perturbed by GWs. Due to the nonlinear relationship between the chemical heating generation and GW perturbations, even a non-breaking GWs can potentially induce non-zero heat flux and alter the background thermal structure.

In this study, simulation of the breaking of a single high-frequency GW packet shows very little heat flux. Further studies are required to take into account of multiple simultaneous GW breakings under more general background conditions and at multiple temporal and spatial scales. This will help ascertain the effects of wave-wave and wave/mean-flow interactions, instabilities, and turbulence accompanying superposed GWs breaking events, that may impact the thermal structure thus contributing to the MIL formation (e.g., Fritts & Wang, 2013).

5. Summary and Conclusion

The Complex Geometry Compressible Atmosphere Model (CGCAM) was employed here to explore the propagation and instability dynamics of 2-D and 3-D GW packets entering highly structured ducting environments (MIL and TW) enabling GW ducting. Two types of cases were considered, one for small-amplitude GWs, and the other for large-amplitude GWs. Results of our simulations for the small-amplitude GWs (Cases 1a, 2a, and 3a) include the following:

1. Trapped GWs in the duct satisfy the relationship $\lambda_z = 2h/n$, for $n = 1, 2, 3$, etc., (referred to as zero, first, and second wave mode, respectively), where λ_z is the local vertical wavelength of the trapped GWs, and h is the duct width;

2. The morphology of trapped GWs directly is dictated by the ducting strength. The stronger the ducting environments, the greater the possibility of exciting higher order trapped modes, and stronger ducting reduces transmitted GW amplitudes.

Results for large-amplitude GWs (Cases 1b, 1c, 2b, and 3b) include the following:

1. Localized GWs undergoing breaking and/or SA dynamics exhibit complex dynamics in the presence of highly structured (i.e., ducting) environments. Responses include reflection, trapping, transmission, 2-D and 3-D instabilities, induced transient mean flows, variable momentum transport and deposition, and SGW and AW responses at higher altitudes;

2. Highly structured ducting environments exhibit strong modulations of primary GWs and SGWs. High-frequency SGWs emitted from strong instabilities in ducts, and SGWs that arise from transmitted GWs, have large scales and large influences extending to much higher altitudes;

3. Ducts enhance GW amplitudes due to compression of their vertical wavelengths accompanying m^2 approaches 0, this causes the GWs to achieve breaking amplitudes below where they would otherwise arise;

4. Stronger ducts cause more efficient GW reflection, thus less energy enters the ducts from below and weaker GWs propagate to higher altitudes;

5. Interactions between GWs and ducts yield layering in the mean wind, and mean wind accelerations are largely contributed by 2-D GW dynamics rather than 3-D instabilities, and the increasing convergence between the

ducting level and the stable region below accelerates the mean flow and extends the shear layer to lower altitudes; and

6. GW breaking and instability dynamics in the ducts do not yield strong net heating/cooling in the thermal structure, this suggests that GW-induced heat transport might not be as strong as previously argued by some authors.

The present numerical simulations with advanced model configurations confirm previous finding that MIL generation may not be caused by the breaking of a transient high-frequency GW packet alone. Both simulations in F18 and this paper are based on the interaction between a high-frequency GW and a duct. This similarity indicates that heat fluxes caused by transient high-frequency GW packets are too small. However, this may be different for mid-frequency GWs and more turbulent environments. It is anticipated that high-resolution CGCAM modeling can provide additional insights into MIL formation mechanisms for other GW and initial flow specifications. Further assessments of GW influences on evolving mean wind and thermal fields will hopefully contribute to improved GW parameterizations in general circulation, and weather and climate prediction models.

Data Availability Statement

Our simulation data is stored and provided at https://doi.org/10.6084/m9.figshare.14701647.v1. Simulation data is provided in *vtk* format and can be opened by the open source software ParaView version 5.10 (Ahrens et al., 2005; Ayachit, 2015), which is available under the BSD license at https://www.paraview.org/download/. ParaView Guide can be downloaded from the ParaView website http://www.paraview.org/download/.

References

Abdilghanie, A. M., & Diamessis, P. J. (2013). The internal gravity wave field emitted by a stably stratified turbulent wake. *Journal of Fluid Mechanics*, *720*, 104–139. https://doi.org/10.1017/jfm.2012.640

Ahrens, J., Geveci, B., & Law, C. (2005). *ParaView: An end-user tool for large data visualization, visualization handbook*. Elsevier. https://doi.org/10.1016/B978-012387582-2/50038-1

Alexander, M. J., & Barnet, C. (2007). Using satellite observations to constrain parameterizations of gravity wave effects for global models. *Journal of the Atmospheric Sciences*, *64*(5), 1652–1665. https://doi.org/10.1175/JAS3897.1

Ayachit, U. (2015). *The paraview guide: A parallel visualization application*. Kitware.

Baumgarten, G., & Fritts, D. C. (2014). Quantifying Kelvin-Helmholtz instability dynamics observed in noctilucent clouds: 1. Methods and observations. *Journal of Geophysical Research: Atmospheres*, *119*, 9324–9337. https://doi.org/10.1002/2014JD021832

Baumgarten, K., Gerding, M., & Lübken, F. J. (2017). Seasonal variation of gravity wave parameters using different filter methods with daylight lidar measurements at midlatitudes. *Journal of Geophysical Research*, *122*(5), 2683–2695. https://doi.org/10.1002/2016JD025916

Bühler, O., McIntyre, M. E., & Scinocca, J. F. (1999). On shear-generated gravity waves that reach the mesosphere. Part I: Wave generation. *Journal of the Atmospheric Sciences*, *56*(21), 3749–3763. https://doi.org/10.1175/1520-0469(1999)056<3749:OSGGWT>2.0.CO;2

Cao, B., Heale, C. J., Guo, Y., Liu, A. Z., & Snively, J. B. (2016). Observation and modeling of gravity wave propagation through reflection and critical layers above Andes Lidar observatory at Cerro Pachón, Chile. *Journal of Geophysical Research*, *121*(21), 12737–12750. https://doi.org/10.1002/2016JD025173

Chen, C., Chu, X., Zhao, J., Roberts, B. R., Yu, Z., Fong, W., & Smith, J. A. (2016). Lidar observations of persistent gravity waves with periods of 3–10 hr in the Antarctic middle and upper atmosphere at McMurdo (77.83°S, 166.67°E). *Journal of Geophysical Research: Space Physics*, *121*(2), 1483–1502. https://doi.org/10.1002/2015JA022127

Chimonas, G., & Grant, J. R. (1984a). Shear excitation of gravity waves. Part 1: Modes of a two-scale atmosphere. *Journal of the Atmospheric Sciences*, *41*(15), 2269–2277. https://doi.org/10.1175/1520-0469(1984)041<2269:SEOGWP>2.0.CO;2

Chimonas, G., & Grant, J. R. (1984b). Shear excitation of gravity waves. Part 2: Upscale scattering from Kelvin-Helmholtz waves. *Journal of the Atmospheric Sciences*, *41*(15), 2278–2288. https://doi.org/10.1175/1520-0469(1984)041<2278:SEOGWP>2.0.CO;2

Chimonas, G., & Hines, C. O. (1986). Doppler ducting of atmospheric gravity waves. *Journal of Geophysical Research*, *91*(D1), 1219. https://doi.org/10.1029/jd091id01p01219

Coy, L., & Fritts, D. C. (1988). Gravity wave heat fluxes: A Lagrangian approach. *Journal of the Atmospheric Sciences*, *45*(12), 1770–1780. https://doi.org/10.1175/1520-0469(1988)045<1770:GWLFAL>2.0.CO;2

Dewan, E. M., & Picard, R. H. (1998). Mesospheric bores. *Journal of Geophysical Research*, *103*(D6), 6295–6305. https://doi.org/10.1029/97JD02498

Dewan, E. M., & Picard, R. H. (2001). On the origin of mesospheric bore. *Journal of Geophysical Research*, *106*, 2921–2927. https://doi.org/10.1029/2000JD900697

Dong, W., Fritts, D. C., Lund, T. S., Wieland, S. A., & Zhang, S. (2020). Self-acceleration and instability of gravity wave packets: 2. Two-dimensional packet propagation, instability dynamics, and transient flow responses. *Journal of Geophysical Research: Atmospheres*, *125*, e2019JD030691. https://doi.org/10.1029/2019JD030691

Dong, W., Fritts, D. C., Thomas, G. E., & Lund, T. S. (2021). Modeling responses of polar mesospheric clouds to gravity wave and instability dynamics and induced large-scale motions. *Journal of Geophysical Research: Atmospheres*, *126*, e2021JD034643. https://doi.org/10.1029/2021JD034643

Dong, W., Hickey, M. P., & Zhang, S. (2021). A numerical study of gravity waves propagation characteristics in the mesospheric Doppler duct. *Journal of Geophysical Research: Atmospheres*, *126*, e2021JD034680. https://doi.org/10.1029/2021JD034680

Dong, W., Zhang, S., Huang, C., Huang, K., Gong, Y., & Gan, Q. (2018). A numerical study of gravity wave propagation characteristics in the stratospheric thermal duct. *Journal of Geophysical Research: Atmospheres*, *123*, 11918–11937. https://doi.org/10.1029/2018JD029190

Duck, T. J., Sipler, D. P., Salah, J. E., & Meriwether, J. W. (2001). Rayleigh lidar observations of a mesospheric inversion layer during night and day. *Geophysical Research Letters*, *28*(18), 3597–3600. https://doi.org/10.1029/2001GL013409

Ebel, A. (1984). Contributions of gravity waves to the momentum, heat and turbulent energy budget of the upper mesosphere and lower thermosphere. *Journal of Atmospheric and Terrestrial Physics*, *46*(9), 727–737. https://doi.org/10.1016/0021-9169(84)90054-0

Ern, M., Preusse, P., Gille, J. C., Hepplewhite, C. L., Mlynczak, M. G., Russell, J. M., & Riese, M. (2011). Implications for atmospheric dynamics derived from global observations of gravity wave momentum flux in stratosphere and mesosphere. *Journal of Geophysical Research*, *116*(19), D05102. https://doi.org/10.1029/2011JD015821

Fadnavis, S., & Beig, G. (2004). Mesospheric temperature inversions over the Indian tropical region. *Annales Geophysicae*, *22*(10), 3375–3382. https://doi.org/10.5194/angeo-22-3375-2004

Felten, F. N., & Lund, T. S. (2006). Kinetic energy conservation issues associated with the collocated mesh scheme for incompressible flow. *Journal of Computational Physics*, *215*, 465–484. https://doi.org/10.1016/j.jcp.2005.11.009

France, J. A., Harvey, V. L., Randall, C. E., Collins, R. L., Smith, A. K., Peck, E. D., & Fang, X. (2015). A climatology of planetary wave-driven mesospheric inversion layers in the extratropical winter. *Journal of Geophysical Research: Atmospheres*, *120*, 399–413. https://doi.org/10.1002/2014JD022244

Fritts, D. C. (1982). Shear excitation of atmospheric gravity waves. *Journal of the Atmospheric Sciences*, *39*(9), 1936–1952. https://doi.org/10.1175/1520-0469(1982)039<1936:SEOAGW>2.0.CO;2

Fritts, D. C. (1984). Shear excitation of atmospheric gravity waves. Part II: Nonlinear radiation from a free shear layer. *Journal of the Atmospheric Sciences*, *41*(4), 524–537. https://doi.org/10.1175/1520-0469(1984)041<0524:SEOAGW>2.0.CO;2

Fritts, D. C., & Alexander, M. J. (2003). Gravity wave dynamics and effects in the middle atmosphere. *Reviews of Geophysics*, *41*, 1003. https://doi.org/10.1029/2001RG000106

Fritts, D. C., Dong, W., Lund, T. S., Wieland, S., & Laughman, B. (2020). Self-acceleration and instability of gravity wave packets: 3. Three-dimensional packet propagation, secondary gravity waves, momentum transport, and transient mean forcing in tidal winds. *Journal of Geophysical Research: Atmospheres*, *125*(3), e2019JD030692. https://doi.org/10.1029/2019JD030692

Fritts, D. C., & Dunkerton, T. J. (1984). Quasi-linear study of gravity wave saturation and self-acceleration. *Journal of the Atmospheric Sciences*, *41*(22), 3272–3289. https://doi.org/10.1175/1520-0469(1984)041<3272:AQLSOG>2.0.CO;2

Fritts, D. C., & Dunkerton, T. J. (1985). Fluxes of heat and constituents due to convectively unstable gravity waves. *Journal of the Atmospheric Sciences*, *42*(6), 549–556. https://doi.org/10.1175/1520-0469(1985)042<0549:FOHACD>2.0.CO;2

Fritts, D. C., Isler, J. R., Thomas, G. E., & Andreassen, Ø. (1993). Wave breaking signatures in noctilucent clouds. *Geophysical Research Letters*, *20*(19), 2039–2042. https://doi.org/10.1029/93GL01982

Fritts, D. C., Laughman, B., Lund, T. S., & Snively, J. B. (2015). Self-acceleration and instability of gravity wave packets: 1. Effects of temporal localization. *Journal of Geophysical Research*, *120*(17), 8783–8803. https://doi.org/10.1002/2015JD023363

Fritts, D. C., Laughman, B., Wang, L., Lund, T. S., & Collins, R. L. (2018). Gravity wave dynamics in a mesospheric inversion layer: 1. Reflection, trapping, and instability dynamics. *Journal of Geophysical Research: Atmospheres*, *123*, 626–648. https://doi.org/10.1002/2017JD027440

Fritts, D. C., & Li, Y. (1989). An analysis of gravity wave ducting in the atmosphere: Eckart's resonances in thermal and Doppler ducts. *Journal of Geophysical Research*, *94*(D15), 18455–18466. https://doi.org/10.1029/jd094id15p18455

Fritts, D. C., Miller, A. D., Kjellstrand, C. B., Geach, C., Williams, B. P., Kaifler, B., & Randall, C. E. (2019). PMC Turbo: Studying gravity wave and instability dynamics in the summer mesosphere using polar mesospheric cloud imaging and profiling from a stratospheric balloon. *Journal of Geophysical Research: Atmospheres*, *124*(12), 6423–6443. https://doi.org/10.1029/2019JD030298

Fritts, D. C., & Wang, L. (2013). Gravity wave-fine structure interactions. Part II: Energy dissipation evolutions, statistics, and implications. *Journal of the Atmospheric Sciences*, *70*(12), 3735–3755. https://doi.org/10.1175/JAS-D-13-059.1

Fritts, D. C., Wang, L., Laughman, B., Lund, T. S., & Collins, R. L. (2018). Gravity wave dynamics in a mesospheric inversion layer: 2. Instabilities, turbulence, fluxes, and mixing. *Journal of Geophysical Research: Atmospheres*, *123*, 649–670. https://doi.org/10.1002/2017JD027442

Gan, Q., Zhang, S. D., & Yi, F. (2012). TIMED/SABER observations of lower mesospheric inversion layers at low and middle latitudes. *Journal of Geophysical Research: Atmosphere*, *117*, D07109. https://doi.org/10.1029/2012JD017455

Garcia, R. R., Smith, A. K., Kinnison, D. E., de la Cámara, Á., & Murphy, D. J. (2017). Modification of the gravity wave parameterization in the whole atmosphere community climate model: Motivation and results. *Journal of the Atmospheric Sciences*, *74*(1), 275–291. https://doi.org/10.1175/JAS-D-16-0104.1

Gardner, C. S., & Liu, A. Z. (2007). Seasonal variations of the vertical fluxes of heat and horizontal momentum in the mesopause region at Starfire Optical Range, New Mexico. *Journal of Geophysical Research*, *112*(9), D09113. https://doi.org/10.1029/2005JD006179

Gardner, C. S., & Yang, W. (1998). Measurements of the dynamical cooling rate associated with the vertical transport of heat by dissipating gravity waves in the mesopause region at the Starfire Optical Range, New Mexico. *Journal of Geophysical Research*, *103*(D14), 16909–16926. https://doi.org/10.1029/98JD00683

Germano, M., Piomelli, U., Moin, P., & Cabot, W. H. (1991). A dynamic subgrid-scale eddy viscosity model. *Physics of Fluids A*, *3*(7), 1760–1765. https://doi.org/10.1063/1.857955

Guo, Y., & Liu, A. Z. (2021). Seasonal variation of vertical heat and energy fluxes due to dissipating gravity waves in the mesopause region over the Andes. *Journal of Geophysical Research: Atmospheres*, *126*(3). https://doi.org/10.1029/2020JD033825

Hauchecorne, A., Chanin, M. L., & Wilson, R. (1987). Mesospheric temperature inversion and gravity wave dynamics. *Geophysical Research Letters*, *14*, 935–939. https://doi.org/10.1029/GL014i009p00933

Heale, C. J., Snively, J. B., & Hickey, M. P. (2014). Numerical simulation of the long-range propagation of gravity wave packets at high latitudes. *Journal of Geophysical Research: Atmospheres*, *119*(19), 11116–11134. https://doi.org/10.1002/2014JD022099

Hecht, J. H., Fritts, D. C., Gelinas, L. J., Rudy, R. J., Walterscheid, R. L., & Liu, A. Z. (2020). Kelvin-Helmholtz billow interactions and instabilities in the mesosphere over the Andes Lidar observatory: 1. Observations. *Journal of Geophysical Research: Atmospheres*, *126*, e2020JD033414. https://doi.org/10.1029/2020JD033414

Hecht, J. H., Liu, A. Z., Walterscheid, R. L., & Rudy, R. J. (2005). Maui Mesosphere and Lower Thermosphere (Maui MALT) observations of the evolution of Kelvin-Helmholtz billows formed near 86 km altitude. *Journal of Geophysical Research*, *110*, D09S10. https://doi.org/10.1029/2003JD003908

Hindley, N. P., Wright, C. J., Hoffmann, L., Moffat-Griffin, T., & Mitchell, N. J. (2020). An 18-year climatology of directional stratospheric gravity wave momentum flux from 3-D satellite observations. *Geophysical Research Letters*, *47*(22), e2020GL089557. https://doi.org/10.1029/2020GL089557

Huang, T. Y., Hickey, M. P., Tuan, T.-F., Dewan, E. M., & Picard, R. H. (2002). Further investigations of a mesospheric inversion layer observed in the ALOHA-93 campaign. *Journal of Geophysical Research*, *107*(D19), 4408. https://doi.org/10.1029/2001JD001186

Huang, T. Y., Hur, H., Tuan, T. F., Li, X., Dewan, E. M., & Picard, R. H. (1998). Sudden narrow temperature-inversion-layer formation in ALOHA-93 as a critical-layer-interaction phenomenon. *Journal of Geophysical Research*, *103*, 6323–6332. https://doi.org/10.1029/97JD03076

Kaifler, N., Kaifler, B., Dörnbrack, A., Rapp, M., Hormaechea, J. L., & de la Torre, A. (2020). Lidar observations of large-amplitude mountain waves in the stratosphere above Tierra del Fuego, Argentina. *Scientific Reports*, *10*(1), 1–10. https://doi.org/10.1038/s41598-020-71443-7

Kaifler, N., Kaifler, B., Ehard, B., Gisinger, S., Dörnbrack, A., Rapp, M., et al. (2017). Observational indications of downward-propagating gravity waves in middle atmosphere Lidar data. *Journal of Atmospheric and Solar-Terrestrial Physics*, *162*, 16–27. https://doi.org/10.1016/j.jastp.2017.03.003

Klostermeyer, J. (1991). Two- and three-dimensional parametric instabilities in finite-amplitude internal gravity waves. *Geophysical & Astrophysical Fluid Dynamics*, *61*(1–4), 1–25. https://doi.org/10.1080/03091929108229035

Larsen, M. F. (2002). Winds and shears in the mesosphere and lower thermosphere: Results from four decades of chemical release wind measurements. *Journal of Geophysical Research*, *107*(A8), SIA-28. https://doi.org/10.1029/2001JA000218

Li, T., She, C. Y., Liu, H. L., Leblanc, T., & McDermid, I. S. (2007). Sodium lidar-observed strong inertia-gravity wave activities in the mesopause region over Fort Collins, Colorado (41°N, 105°W). *Journal of Geophysical Research*, *112*(22), 15. https://doi.org/10.1029/2007JD008681

Liu, H.-L., & Hagan, M. E. (1998). Local heating/cooling of the mesosphere due to gravity wave and tidal coupling. *Geophysical Research Letters*, *25*, 2941–2944. https://doi.org/10.1029/98GL02153

Liu, H.-L., Hagan, M. E., & Roble, R. G. (2000). Local mean state changes due to gravity wave breaking modulated by the diurnal tide. *Journal of Geophysical Research*, *105*, 12381–12396. https://doi.org/10.1029/1999JD901163

Liu, H. L., Hays, P. B., & Roble, R. G. (1999). A numerical study of gravity wave breaking and impacts on turbulence and mean state. *Journal of the Atmospheric Sciences*, *56*(13), 2152–2177. https://doi.org/10.1175/1520-0469(1999)056<2152:ANSOGW>2.0.CO;2

Liu, X., Yue, J., Xu, J., Garcia, R. R., Russell, J. M., Mlynczak, M., & Nakamura, T. (2017). Variations of global gravity waves derived from 14 years of SABER temperature observations. *Journal of Geophysical Research*, *122*(12), 6231–6249. https://doi.org/10.1002/2017JD026604

Lombard, P. N., & Riley, J. J. (1996). On the breakdown into turbulence of propagating internal waves. *Dynamics of Atmospheres and Oceans*, *23*(1–4), 345–355. https://doi.org/10.1016/0377-0265(95)00431-9

Lund, T. S., Fritts, D. C., Wan, K., Laughman, B., & Liu, H. (2020). Numerical simulation of mountain waves over the Southern Andes. Part 1: Mountain wave and secondary wave character, evolutions, and breaking. *Journal of the Atmospheric Sciences*, 4337–4356. https://doi.org/10.1175/JAS-D-19-0356.1

McIntyre, M. E. (1989). On dynamics and transport near the polar mesopause in summer. *Journal of Geophysical Research*, *94*(D12), 14617–14628. https://doi.org/10.1029/jd094id12p14617

Medvedev, A. S., & Klassen, G. P. (2003). Thermal effects of saturating gravity waves in the atmosphere. *Journal of Geophysical Research*, *108*(D2), 4040. https://doi.org/10.1029/2002JD002504

Meriwether, J. W., & Gardner, C. S. (2000). A review of the mesospheric inversion layer phenomenon. *Journal of Geophysical Research*, *105*(D10), 12405–12416. https://doi.org/10.1029/2000JD900163

Meriwether, J. W., & Gerrard, A. J. (2004). Mesosphere inversion layers and stratosphere temperature enhancements. *Reviews of Geophysics*, *42*(3). https://doi.org/10.1029/2003RG000133

Meriwether, J. W., & Mlynczak, M. G. (1995). Is chemical heating a major cause of the mesosphere inversion layer? *Journal of Geophysical Research*, *100*(D1), 1379–1387. https://doi.org/10.1029/94JD01736

Moin, P., Squires, K. D., Cabot, W. H., & Lee, S. (1991). A dynamic subgrid-scale model for compressible turbulence and scalar transport. *Physics of Fluids A*, *3*(11), 2746–2757. https://doi.org/10.1063/1.858164

Murphy, D. J., Alexander, S. P., Klekociuk, A. R., Love, P. T., & Vincent, R. A. (2014). Radiosonde observations of gravity waves in the lower stratosphere over Davis, Antarctica. *Journal of Geophysical Research*, *119*(21), 11973–11996. https://doi.org/10.1002/2014JD022448

Pautet, P.-D., Taylor, M. J., Fritts, D. C., Janches, D., Kaifler, N., Dörnbrack, A., & Hormaechea, J. L. (2021). Mesospheric mountain wave activity in the lee of the Southern Andes. *Journal of Geophysical Research: Atmospheres*, *126*, e2020JD033268. https://doi.org/10.1029/2020JD033268

Pautet, P.-D., Taylor, M. J., Pendleton, W. R., Zhao, Y., Yuan, T., Esplin, R., & McLain, D. (2014). Advanced mesospheric temperature mapper for high-latitude airglow studies. *Applied Optics*, *53*(26), 5934. https://doi.org/10.1364/ao.53.005934

Snively, J. B., & Pasko, V. P. (2004). Breaking of thunderstorm-generated gravity waves as a source of short-period ducted waves at mesopause altitudes. *Geophysical Research Letters*, *30*(24), 285–295. https://doi.org/10.1029/2003GL018436

Snively, J. B., Pasko, V. P., Taylor, M. J., & Hocking, W. K. (2007). Doppler ducting of short-period gravity waves by midlatitude tidal wind structure. *Journal of Geophysical Research*, *112*(A3), A03304. https://doi.org/10.1029/2006JA011895

Stephan, C. C., Lane, T. P., & Jakob, C. (2020). Gravity wave influences on mesoscale divergence: An observational case study. *Geophysical Research Letters*, *47*(1), e2019GL086539. https://doi.org/10.1029/2019GL086539

Strobel, D. F., Apruzese, J. P., & Schoeberl, M. R. (1985). Energy balance constraints on gravity wave induced eddy diffusion in the mesosphere and lower thermosphere. *Journal of Geophysical Research*, *90*(D7), 13067–13072. https://doi.org/10.1029/JD090iD07p13067

Strobel, D. F., Summers, M. E., Bevilacqua, R. M., Deland, M. T., & Allen, M. (1987). Vertical constituent transport in the mesosphere. *Journal of Geophysical Research*, *92*(D6), 6691–6698. https://doi.org/10.1029/JD092iD06p06691

Sutherland, B. R. (2001). Finite-amplitude internal wave packet disperson and breaking. *Journal of Fluid Mechanics*, *429*, 343–380. https://doi.org/10.1017/S0022112000002846

Sutherland, B. R. (2006). Internal wave instability: Wave-wave versus wave-induced mean flow interactions. *Physics of Fluids*, *18*(7). https://doi.org/10.1063/1.2219102

Tsuda, T., Ratnam, M. V., May, P. T., Alexander, M. J., Vincent, R. A., & MacKinnon, A. (2004). Characteristics of gravity waves with short vertical wavelengths observed with radiosonde and GPS occultation during DAWEX (Darwin Area Wave Experiment). *Journal of Geophysical Research D: Atmospheres*, *109*(20), D20S03. https://doi.org/10.1029/2004JD004946

Walterscheid, R. L. (1981). Dynamical cooling induced by dissipating internal gravity waves. *Geophysical Research Letters*, *8*(12), 1235–1238. https://doi.org/10.1029/GL008i012p01235

Walterscheid, R. L., & Hickey, M. P. (2009). Gravity wave ducting in the upper mesosphere and lower thermosphere duct system. *Journal of Geophysical Research*, *114*(D19). https://doi.org/10.1029/2008JD011269

White, F. M. (1974). *Viscous fluid flow*. McGraw-Hill.

Yu, Y., & Hickey, M. P. (2007a). Numerical modeling of a gravity wave packet ducted by the thermal structure of the atmosphere. *Journal of Geophysical Research*, *112*(A6), A06308. https://doi.org/10.1029/2006JA012092

Yu, Y., & Hickey, M. P. (2007b). Simulated ducting of high-frequency atmospheric gravity waves in the presence of background winds. *Geophysical Research Letters*, *34*(34). https://doi.org/10.1029/2007GL029591

Yue, J., Vadas, S. L., She, C. Y., Nakamura, T., Reising, S. C., Liu, H. L., & Li, T. (2009). Concentric gravity waves in the mesosphere generated by deep convective plumes in the lower atmosphere near Fort Collins, Colorado. *Journal of Geophysical Research*, *114*(6), D06104. https://doi.org/10.1029/2008JD011244

Zhang, S. D., Huang, C. M., Huang, K. M., Yi, F., Zhang, Y. H., Gong, Y., & Gan, Q. (2014). Spatial and seasonal variability of medium-and high-frequency gravity waves in the lower atmosphere revealed by US radiosonde data. *Annales Geophysicae*, *32*(9), 1129–1143. https://doi.org/10.5194/angeo-32-1129-2014

Zhang, S. D., Yi, F., Huang, C. M., Huang, K. M., Gan, Q., Zhang, Y. H., & Gong, Y. (2013). Latitudinal and altitudinal variability of lower atmospheric inertial gravity waves revealed by U.S. radiosonde data. *Journal of Geophysical Research: Atmospheres*, *118*(14), 7750–7764. https://doi.org/10.1002/jgrd.50623